12

AD

AD-E402 638

Technical Report ARCCD-TR-94003

EFFECT OF AUSTEMPER HEAT TREATMENT ON WELD HEAT AFFECTED ZONES OF CAST DUCTILE IRON

Stephen Luckowski
George Scullin
Roger Stanton

May 1995

US ARMY
TANK AUTOMOTIVE AND
ARMAMENTS COMMAND
ARMAMENT RDE CENTER

U.S. ARMY ARMAMENT RESEARCH, DEVELOPMENT AND ENGINEERING CENTER

Close Combat Armaments Center
Armament Engineering Directorate

Picatinny Arsenal, New Jersey

The views, opinions, and/or findings contained in this report are those of the authors(s) and should not be construed as an official Department of the Army position, policy, or decision, unless so designated by other documentation.

The citation in this report of the names of commercial firms or commercially available products or services does not constitute official endorsement by or approval of the U.S. Government.

Destroy this report when no longer needed by any method that will prevent disclosure of its contents or reconstruction of the document. Do not return to the originator.

ERRATA

Technical Report ARCCD-TR-94003

EFFECT OF AUSTEMPER HEAT TREATMENT ON WELD HEAT AFFECTED ZONES OF CAST DUCTILE IRON

Stephen Luckowski
George Scullin
Roger Stanton

May 1995

Please add to figure titles 6 through 23, 26 through 28, and 30 through 33 -- 500 times.

Please add to figure title 37 -- 545 times.

Please add to figure title 29 -- 1000 times.

June 1995

REPORT DOCUMENTATION PAGE

Form Approved OMB No. 0704-0188

1. AGENCY USE ONLY (Leave blank)	2. REPORT DATE	3. REPORT TYPE AND DATES COVERED
	May 1995	

4. TITLE AND SUBTITLE

EFFECT OF AUSTEMPER HEAT TREATMENT ON WELD HEAT AFFECTED ZONES OF CAST DUCTILE IRON

5. FUNDING NUMBERS

6. AUTHOR(S)

Stephen Luckowski, George Scullin, and Roger Stanton

7. PERFORMING ORGANIZATION NAME(S) AND ADDRESSES(S)

ARDEC, CCAC
Heavy Armament Division
(AMSTA-AR-CCH-D)
Picatinny Arsenal, NJ 21005-5001

ARDEC, AED
Materials & Aeroballistics Technology Division (AMSTA-AR-AET-M)

8. PERFORMING ORGANIZATION REPORT NUMBER

9.SPONSORING/MONITORING AGENCY NAME(S) AND ADDRESS(S)

ARDEC, DOIM
Information Research Center (AMSTA-AR-IMC)
Picatinny Arsenal, NJ 07806-5000

10. SPONSORING/MONITORING AGENCY REPORT NUMBER

Technical Report
ARCCD-TR-940003

11. SUPPLEMENTARY NOTES

12a. DISTRIBUTION/AVAILABILITY STATEMENT

Approved for public release; distribution is unlimited.

12b. DISTRIBUTION CODE

13. ABSTRACT (Maximum 200 words)

This report is the first of a three year Army Manufacturing, Science, and Technology (MS&T) Congressionally mandated effort to investigate the weldability of a specific grade of austempered ductile iron (ADI). This specific grade of ductile iron was developed under MS&T project 5904948 and has mechanical properties after austemper heat treatment of 140,000 psi minimum yield strength and 8% minimum elongation.

This report describes the use of the Gleeble experimental technique to produce the thermal cycles experienced in welding, thus creating simulated weld heat affected zones (HAZ). Simulated HAZ were produced for two different weld energy inputs and five weld preheat temperatures. Weldability was assessed by measuring resultant hardness and through microstructural observations of the as-welded and subsequently austempered material. Results of this work provide a foundation of knowledge in the as-welded heat affected zone, determine the extent of recovery of the weld (HAZ) due to subsequent austemper heat treatment, and provide information on suitable preheat temperatures and weld energy inputs for actual weld trials.

14. SUBJECT TERMS				15. NUMBER OF PAGES 60
Gleeble	As-welded	Austemper	Cast ductile iron	16. PRICE CODE

17. SECURITY CLASSIFICATION OF REPORT	18. SECURITY CLASSIFICATION OF THIS PAGE	19. SECURITY CLASSIFICATION OF ABSTRACT	20. LIMITATION OF ABSTRACT
UNCLASSIFIED	UNCLASSIFIED	UNCLASSIFIED	SAR

CONTENTS

FIGURES

FIGURES (cont)

FIGURES (cont)

FIGURES (cont)

INTRODUCTION

This is a report on the first year of a 3 year effort to investigate the weldability of austempered ductile iron (ADI). This project is a task under the Army Manufacturing Science and Technology (MS&T) Ductile Iron Program in response to Congressionally directed Army, Navy, and Air Force MS&T initiatives to explore military and industrial uses of American ductile iron. In FY 92, the overall Army program encompassed projects in three distinct areas: projectile applications, vehicle applications, and continued exploration of uses for American ductile iron in defense related applications. It is under this third area that the first year of a 3 year effort was initiated.

The 3 year effort was designed to investigate the weldability of a specific grade of ductile iron, as welding must be considered as a fabrication technique in its potential applications. The term ductile iron as used in this report refers to a specific chemistry of ductile iron which responds to austempering heat treatment. The first year was designed to provide the foundation knowledge for the second and third year as well as to provide information for another MS&T project on the application of overlay welded copper alloy rotating bands to ductile iron artillery projectiles. The first year investigated the effect thermal cycling, due to welding, has on the microstructure of as-cast ductile iron and the effect a subsequent austemper heat treatment has on the heat-affected microstructure. This applies to applications where austemper heat treatment can be performed after welding. The information generated by the first year effort will be used to execute the second and third year efforts. Results will be used to select preheat temperatures for actual welding trials and will be used in subsequent analysis of the weld heat affected zones. The second year project will investigate fusion welding of ductile iron using the gas metal arc welding (GMAW) process. This will consist of using various filler metals and two energy inputs to evaluate resultant mechanical properties of both the as-welded austempered ductile iron and welded ADI with subsequent austemper heat treatment. This second year work is designed to apply to both field repair and production fabrication of ductile iron components. The third year will investigate the effect thermal cycling, due to welding, has on the microstructure of ductile iron, which has been austempered heat treated prior to welding. This applies to components which cannot be heat treated after welding. The third year will also investigate solid state welding of ductile iron before and after austemper heat treatment using friction (inertia) welding.

Austempered ductile iron is a family of alloys developed by the American ductile iron industry which possess mechanical properties through an austemper heat treatment comparable to alloy steel. The austemper heat treatment is essentially the distinguishing feature of this family of alloys when compared to standard grades of ductile iron. The austemper heat treatment produces an arrested bainitic microstructure, a mixture of bainitic ferrite and high carbon retained austenite, which is primarily responsible for the enhanced mechanical properties of austempered ductile iron (ref 1). The austemper heat treatment cycle is sensitive to many material related factors,

such as: nodule size and distribution, alloy content, and alloy distribution to prevent formation of pearlite upon quenching. These factors require manipulation of austenitizing parameters, namely austenitizing temperature and time and quench medium temperature and time in quench to achieve the optimum desired microstructure.

Work by Nippes, et al, demonstrated that ductile iron exhibits many complex reactions when exposed to the thermal cycles experienced during welding which are responsible for forming brittle constituents such as martensite and massive carbide, and that these constituents were not necessarily avoidable even through employing preheat (ref 2). Since austempered ductile iron would not be used in the as-welded condition as investigated by Nippes, the first year effort investigated the effect these constituents have on the resultant austempered microstructure--that is, whether the as-welded microstructure is recoverable through austemper heat treatment.

The experimental technique used to perform this work was the same as that used by Nippes, et al. A synthetic specimen technique, using a machine known as the Gleeble, was used to produce simulated weld thermal cycles duplicating preheat and peak temperatures achieved in the weld heat affected zone (HAZ). The experimental plan expands on Nippes work by examining not only the effect of preheat temperature on heat affected zone microstructure and hardness, but also by examining the effect of weld energy input and subsequent austemper heat treatment on HAZ microstructure and hardness.

The specific alloy selected for evaluation under this effort is the same alloy that was selected for related MS&T ductile iron projects involving projectile applications. This alloy is not available through commercial specifications and was developed specifically to meet the mechanical properties required for large calibre projectile bodies.

Procedure

The experimental plan was designed to simulate two separate welding procedures which could be used for welding a 0.50 in. plate. Two different weld energy inputs, 37.5 kJ/in. and 22.5 kJ/in., were selected for this investigation. The 37.5 kJ/in. simulates a three pass GWAW using 0.045 in. electrode wire in a 0.50 in. thick plate and the 22.5 kJ/in. simulates a five pass GMAW using 0.045 in. electrode wire in a 0.50 in. thick plate.

The Gleeble synthetic specimen technique enables the examination of the microstructure at any desired point in the heat affected zone which is otherwise difficult to distinguish when examining an entire weld heat affected zone. The simulated thermal cycle of each specimen represents a discrete section of a weld heat affected zone at a predetermined peak temperature. Peak temperatures of 1200°F, 1550°F, 1800°F, 1950°F, 2020°F, and 2100°F were selected. The peak temperatures were

chosen as temperatures at which microstructural and or material property changes could be expected. Figure 1 is a calculated 2-D representation of the weld heat affected zone and corresponding peak temperature profile for the 37.5 kJ/in. and 22.5 kJ/in. energy input.

Five initial preheat temperatures were also selected for both of the weld energy inputs. The preheat temperatures were chosen as those which could be typically used in standard welding practice and have an effect on the resultant microstructures by changing the cooling rate of the heat affected zone. Since cooling rate is a function of part geometry, preheat temperature, and energy input, the plate preheat temperatures actually represent five different cooling rates for each energy input.

The Gleeble synthetic specimen technique was used to produce simulated weld thermal cycles in reduced cross section 10 mm diameter ductile iron bars. Figure 2 is a drawing of the test specimen used in the Gleeble and figure 3 is a photograph of the Gleeble test configuration. Note in figure 3, both the copper jaws and the thermocouple attached at the specimen midsection. The copper jaws allow for both electrical conductivity to heat the specimen and thermal conductivity to cool the specimen. The thermocouple measures both peak temperature and temperature upon cooling. The cooling rate is controlled by pulsing the electrical current.

Cooling rates were measured as the slope of the cooling curve at 1300°F which is the temperature in the region of the pearlite nose on the continuous cooling curve. This temperature was chosen since the cooling rate in this area can be related to the types and amounts of transformation products observed in the treated specimen.

The cooling curves used in this work were mathematically derived from the Rykalin 2-D expression (appendix). Figure 4 is an example of the experimentally determined cooling curves derived from this expression at the 1800°F peak temperature for 72°F and 800°F preheat temperatures showing the difference in cooling rates as influenced by preheat temperatures. Separate cooling curves were generated for each thermal cycle condition. The Gleeble synthetic specimen technique duplicates the cooling curves derived from the Rykalin expression through real-time pulsing of the current with thermocouple feedback control. Thus, a constant cooling rate can be maintained for a given energy input and specimen geometry over the range of peak temperatures for each preheat temperature. Figure 5 summarizes the experimental matrix, showing the combinations of preheat and peak temperatures for the 37.5 kJ/in. and 22.5 kJ/in. weld energy inputs.

Two specimens were thermally cycled for each condition in the matrix. One specimen from each of these conditions was subsequently austempered heat treated. Microstructural observations and hardness measurements were used to evaluate the material in the as-welded and subsequently austempered conditions.

The peak temperatures chosen represent the heat affected zone up to the fusion zone of the weld. The highest peak temperature (2100°F) is just slightly above the nil strength temperature of ductile iron (measured to be 2057°F). Tests above 2100°F could not be carried out due to the excessive melting of the test specimen. The chosen specimen geometry (constant radius, reduced cross section required for desired cooling rates) did not allow for the use of a quartz crucible which could maintain the integrity of the specimen and allow for fusion zone (FZ) testing.

Microstructural observations were made using both light and scanning electron microscopy from metallographic specimens cut transverse to the mid-section of the reduced section Gleeble specimen. Metallographic specimens were cut at the point to which the Gleeble thermocouple was attached to the specimen mid-section, ensuring that the microstructures reflected the desired peak temperatures and cooling rates.

Hardness measurements were taken using the Rockwell A scale. Rockwell A was selected based on information from the reference 1. The Rockwell A scale covers a sufficient area of both nodules and matrix structure. This reduces scatter in hardness readings due to preferential indentation of either the matrix structure or nodules as would occur with microhardness testing.

Material

The material for this work was supplied by Wagner Casting Company of Decatur, Illinois. The specific austempered ductile iron alloy selected for evaluation is the same alloy that was selected for MS&T project 5904948 to investigate using ADI for the 155-mm M864 projectile body of which Wagner Casting was the prime contractor. This alloy is not available through commercial specification. The chemistry, casting process, and heat treatment of the alloy was developed by Wagner in order to meet the M864 mechanical property requirements of a minimum 140 ksi yield strength with an elongation of 8%. As such, the same requirements were specified for this material so the results of this work can be related to other MS&T projects on ADI.

The ADI was provided in the form of a 10-mm diameter bar 12 in. Table 1 shows the nominal chemistry of the material. The bars were comprised from several heats. The chemical composition of each heat used to produce the bars were recorded; however, the supplier did not identify specific bars to the melt chemistries. Therefore, any effect on the results due to variation in the starting material cannot be determined.

The austemper heat treatment was performed by Applied Processes, Inc., a Wagner Casting subcontractor. The parameters used to austemper heat treat the specimens are shown in table 2.

RESULTS

Mechanical Properties

Tensile test results for the austempered as-cast material are shown in table 3. As can be seen from the table the austemper heat treatment performed on this material was satisfactory and the mechanical properties met the desired requirements.

Cooling Rate

The cooling rate results are shown in table 4. These cooling rates were determined as the slope of the cooling curves at 1300°F from Gleeble experimental data. Note that the cooling rates for the 22.5 kJ energy input are approximately 2.8 times as fast as those for the 37.5 kJ/in. energy input. This is due to the size of the respective heat affected zones. The mass of the plate relative to the weld zone for each condition is such that it represents essentially the same heat sink for both conditions. The cooling rates for the two energy inputs differ significantly due to the size of the respective heat affected zones (fig. 1). The cooling rate for any given peak temperature at the lower energy input will be faster since there is less mass heated to the peak temperature than with the higher energy input at the same peak temperature.

The cooling rate is held constant by the Gleeble through the range of peak temperatures at a given preheat temperature for each energy input. In the case of a plate at a given preheat temperature, the heat is removed at a constant rate from the heat affected zone due to the size of the plate versus the size of the weld zone. Effectively, the initial plate temperature does not elevate from the heat of the weld and therefore does not change the cooling rate.

There is some overlap in the cooling rates between the two energy inputs, especially in the 600°F preheat for 37.5 kJ/in. energy input and in the 800°F preheat for 22.5 kJ/in. energy input. This is manifested in similar microstructure and hardness results for the overlapping conditions.

Microstructure

The microstructures formed in austempered ductile iron in both the as-welded and austempered condition can be quite complicated. The carbon nodules represent a source of carbon from which carbon can diffuse into the matrix. The peak temperatures obtained during welding as well as the time above the austenitizing temperature play an important role in the diffusion of carbon into the matrix, thus increasing the carbon concentration of the austenite. This has the effect of increasing the hardenability and decreasing the temperature range of the two phase austenite/ferrite region of the phase diagram upon continuous cooling. Therefore, hardenability and

carbon in solution are a function of the peak temperature reached (ref 2). The cooling rate plays a role in the diffusion of carbon back to the nodules and, of course, amount and type of transformation products.

The microstructures developed during this study will be presented in four categories: 1) as a function of peak temperature reached, as this illustrates the effect the increase in carbon diffusion has on hardenability as the peak temperature increases; 2) as a function of cooling rate, as this illustrates the effect of preheat and energy input have on the amount and type of transformation products at each peak temperature; 3) as a function of post-weld austemper heat treatment; and 4) as a function of the weld partial fusion zone (PFZ) and fusion zone (FZ).

Figure 6 shows the as-cast microstructure in the ductile iron material as received from Wagner at 500x magnification. The as-cast microstructure is essentially a 100% pearlitic structure, with some blocky "bull's eye" ferrite around the graphite nodules.

As-Welded Microstructures

The peak temperature of 1200°F represents a temperature below which the transformation to austenite takes place. Therefore, no transformation on cooling occurs. This microstructure appears exactly as the as-cast structure shown in figure 6 for both the 37.5 and 22.5 kJ/in. energy inputs.

As the peak temperature increases for a given preheat temperature, the rate of carbon diffusion increases and the hardenability of the austenite increases. This is due to the increase in solubility of carbon in austenite and the increase in time at austenitizing temperature. This is most effectively illustrated for a constant cooling rate of 34.5°F/s (37.5 kJ/in. energy input at 72°F preheat temperature) over the range of peak temperatures from 1550°F to 2020°F (figs. 7 through 10). At the peak temperature of 1550°F (fig. 7), the microstructure is ferrite and pearlite with areas of fine pearlite throughout. The peak temperature of 1550°F represents the lowest temperature used in this study at which carbon becomes soluble in austenite. At this temperature, when compared to higher peak temperatures, carbon diffusion is sluggish and solubility in austenite is lower. However, regardless of the peak temperatures, carbon diffusion at the grain boundaries is more rapid than within the austenitic grain. This is evident in the fine pearlite which forms in the vicinity of the prior austenitic grain boundaries. Hardenability due to limited carbon diffusion through the matrix is low, however, as is indicated by a lack of martensite in figure 7. The ferrite present in the photomicrograph is the result of either too short of a time in the austenitic temperature range to promote full austenization, the cooling rate, or a combination of both factors.

As the peak temperature increases (figs. 8 through 10) to 1800°F, 1950°F, and 2020°F respectively, transformation to martensite occurs. At 1800°F, (fig. 8), a mixed microstructure of martensite, pearlite, and ferrite is shown. At 1950°F (fig. 9), a lath-like martensite is evident. At 2020°F (fig. 10), the microstructure is a plate-like martensite

with some retained austenite. One aspect causing this trend is an increase in hardenability due to the increase in carbon content of the austenite as the peak temperature increases. The increase in carbon content also effects the resultant transformed microstructure as discussed previously.

In contrast, cooling rate at a given peak temperature also plays a significant role in the type and amount of transformation products. At a peak temperature of 1550°F, transformation to martensite, ferrite, and pearlite occurred at a cooling rate of 94.5 F/s for the [22.5 kJ/in. energy input, 72°F preheat (fig. 11)]. This can be directly compared to figure 7 where the critical cooling rate was not exceeded and transformation to a fine pearlite at austenitic grain boundaries occurred. At a slower cooling rate (6.3°F/s) at the same peak temperature, transformation to a coarser pearlite and a larger fraction of proeutectoid ferrite occurred (fig. 12).

The increase in hardenability as a function of peak temperature effectively changes the critical cooling rate. This is shown by the various cooling rates which produce martensitic structures at the different peak temperatures. At 1800°F peak temperature, the carbon sufficiently affects the hardenability so that some martensite forms at a cooling rate of 34.0°F/s (fig. 8). At a peak temperature of 1950°F, the hardenability of the austenite increases significantly due to an increase rate of diffusion and amount of carbon into the matrix. Only cooling rates less than 17.5°F/s are sufficient to avoid martensite formation at 1950°F (figs. 13 through 16). It is evident in these figures that as the cooling rate decreases, the microstructure becomes pearlitic. At a peak temperature of 2020°F, solubility of carbon in the austenite is almost at a maximum. This increases hardenability to the point such that a cooling rate of 13.5°F/s or above forms martensite (fig. 17) and only a cooling rate of 6.3°F/s or less can martensite formation be avoided. This is shown in figures 18 through 20.

The slower cooling rates have the additional effect of increasing the time within the austenitic temperature range. This has a subtle effect on uniformity of carbon distribution within the austenite, since longer times within the austenitic region affects rate of carbon diffusion. This is illustrated at a peak temperature of 1800°F. Figures 21 and 22 show fine pearlite in the vicinity of prior austenitic grain boundaries, blocky ferrite, and pearlite at a cooling rate of 6.3°F/s. At the same peak temperature, but at a slower cooling rate (2.3°F/s), a matrix of fine pearlite is evident (fig. 23). The slower cooling rate increases the uniformity of carbon content in austenite and decreases the temperature range of the ferrite/austenite two phase region of the phase diagram throughout the grain, thus forming the fine pearlite of figure 23. At the slightly higher cooling rate of 17.5°F/s (fig. 24), Widmanstätten ferrite and martensite is evident (figs. 24 and 25).

The peak temperature of 2100°F represents the onset of incipient melting that would be exhibited in a PFZ. Both figures 26 and 27 show regions of eutectic carbide, plate martensite, and retained austenite. Grain boundary eutectic carbide is also

apparent in these photomicrographs showing evidence of melting at the grain boundaries. The large area of eutectic in the photomicrographs is due to localized melting at the site of graphite nodules.

Two additional microstructures are included (figs. 28 and 29). The first shows a peak temperature of 2148°F and the other shows a photomicrograph of complete melting. The 2148°F peak temperature was part of some initial work and was not part of the experimental matrix developed, it is included as an example of significant partial fusion zone melting. This figure shows a dendritic structure of transformed ledeburite, having significant amounts of eutectic carbide and martensite due to a near complete dissolution of carbon into the melted regions. Figure 29 is an example of a fusion zone microstructure where near complete dissolution of the graphite nodules occurred. Further examination of the fusion zone was not performed since it is beyond the scope of work for this phase I HAZ effort.

Austempered Microstructure

Figure 30 shows the austempered as-cast microstructure, which is a typical ADI structure of bainitic ferrite and reacted austenite (ref 3). The austempered microstructures are fairly uniform in appearance for all combinations of preheat and peak temperature, with the notable exception of the 2100°F peak temperature (incipient melting). The only difference in appearance is in the fineness of the austempered structure, as is apparent in the comparison of figures 31 and 32. Figures 33 and 34 clearly show the effect of incipient melting in that the graphite nodules are noticeably smaller in size and there is an appearance of areas with larger amounts of austenite presumably where the previous eutectic structure was located. Figures 35 and 36 show a magnified view of this structure at 1000x. Figure 37 shows a scanning electron photomicrograph (backscattered) highlighting the existence of secondary graphite particles.

Hardness

Rockwell A hardness is plotted versus peak temperature for 72°F, 400°F, 600°F, and 800°F preheats. Figures 38 and 39 show the as-welded hardness results for the 37.5 kJ/in. and 22.5 kJ/in. energy inputs, respectively. Figures 40 and 41 show the austempered hardness results for the 37.5 kJ/in. and 22.5 kJ/in. energy inputs, respectively. The variations in the as-welded hardness results show a good correlation to microstructural observations. The austempered hardness results are constant within experimental error.

DISCUSSION

As-welded Condition

As can be seen from the figures presented, a variety of microstructures result from the thermal cycling due to welding. The microstructures will vary depending upon peak temperature and cooling rates affected by the preheat temperature. Due to the rapid heating and cooling rates the diffusion of the carbon is not uniform throughout the austenite. Thus, within the austenitic grain the carbon content and the hardenability of the austenite is not uniform which contributes to the differences in the resultant microstructures throughout the matrix.

Work done by Nippes (ref 1) and Kotecki (ref 4) show that ductile iron is subject to formation of hard and brittle microstructures when exposed to the thermal cycles and cooling rates exhibited in welding, namely martensite, grain boundary carbide, and eutectic carbide. Both of these authors performed this work on standard grades of ferritic ductile iron, which differed both in microstructure and chemistry from the ductile iron in this study. Also, neither author explored post-weld heat treatment to mitigate these structures--only preheat was investigated as a technique to suppress martensite formation. These authors found that though preheat temperature was able to suppress martensite formation, the higher preheat temperatures also increased the amounts of grain boundary carbide (refs 3 and 4).

Results of this work show that grain boundary carbides do not form in ductile iron which has a pearlitic prior microstructure. This is most likely due to the presence of a primarily pearlitic prior microstructure, as compared to the ferritic prior microstructure investigated by the previously mentioned authors. Due to the prevalence of austenitic nucleation sites, a pearlitic matrix is austenitized more easily and allows for carbon diffusion into the austenite grain. Austenitization of ferrite is comparatively slower than pearlite and requires higher austenitizing temperatures. The rapid heating rate during welding will influence the rate and amount of austenite formed depending on the prior microstructure.

In the case of ferritic ductile iron, diffusion of carbon at the grain boundaries occurs with limited diffusion into the matrix until only the highest peak temperatures were reached. The pre-existing ferrite has limited solubility of carbon below the 1800°F peak temperature and suppresses formation of austenite below this temperature. The ferrite effectively arrests the nucleation and growth of austenite below 1800 F because there is limited solubility of carbon in the ferrite and there is little amount of austenite formed. Grain boundary carbides form due to the inability of carbon to sufficiently diffuse through the iron/silicon matrix and form austenite. Above 1800°F in the ferritic prior microstructure, some austenite forms thus increasing the solubility of the matrix for carbon which transforms to martensite or pearlite, depending on the cooling rate. The additional carbon which cannot penetrate the iron/silicon matrix remains as grain boundary carbides.

Diffusion of carbon within the matrix increases with time and temperature due to nucleation and growth of austenite, but diffusion remains limited up to the peak temperature of 2100°F, where incipient melting occurs. Regardless of the peak temperature, intergranular carbides are present in the prior ferritic microstructure.

The prior microstructure in the as-welded conditions affects the degree of austenitization attainable in the matrix, since pearlite is more readily austentized than ferrite. This degree of austenitization affects carbon solubility, hardenability of the austenite, and subsequent transformation products.

The microstructure prior to welding, therefore, influences the subsequent transformation products of the as-welded heat affected zone. A pearlitic prior microstructure does not readily form grain boundary carbides in the HAZ as does a ferritic prior microstructure. For an as-welded structure, this may be important in improving as-welded performance. Although these carbides are most likely recoverable through austemper heat treatment, the absence of their formation is desirable. Limiting the extent to which carbides form in the as-welded structure reduces susceptibility to cracking in the HAZ.

The prior microstructure is dependent on the cooling rate and chemistry of the casting. Therefore, it is difficult to always obtain a pearlitic structure, particularly in large castings with inherently slow cooling rates. Whether or not the prior microstructure is ultimately significant in terms of weldability and subsequent austemper heat treatment, requires further work. It may prove important to know if different procedures are required based on the prior microstructure when welding ductile iron.

The results of this study confirm prior work that preheat is an effective means of suppressing martensite formation in all peak temperatures but the 2100°F case of incipient melting. The preheat required, however, varies as a function of energy input. The lower energy input (22.5 kJ/in.) causes higher cooling rates than the higher energy input process (37.5 kJ/in.), and would require a higher preheat to suppress martensite formation. The resultant microstructures of figures 18 and 20 demonstrate that 6.3°F/s is the critical cooling rate to suppress martensite formation. The suppression of martensite formation is important in the welding of ductile iron components. In order to prevent cracking, martensite formation should be avoided if at all possible. This would require a minimum of a 600°F preheat for the 37.5 kJ/in. energy input, but would be higher for the lower energy input process, 800°F for the 22.5 kJ/in. energy input. This inverse relationship would hold true as energy inputs are decreased; however, increasing preheat will certainly have an effect on the partial fusion zone and fusion zone. Increased preheat will cause more melting in the partial fusion zone and expand the width of the fusion zone, which will increase dissolution of graphite nodules, and thus increase the amount of eutectic carbide.

As in the work by Nippes, the critical cooling rate of the most hardenable austenite was 6.3°F/s (ref 1). The pearlitic prior microstructure in this study, however, was more hardenable through the range of peak temperatures than was the ferritic prior microstructure examined in other studies, as was proposed by Kotecki (ref 4). The pearlitic microstructure has a high carbon content as soon as austenite is formed, whereas the ferritic grades require the diffusion of carbon from the nodules to first allow austenite to form thereby increasing the local carbon concentration and the hardenability. Therefore, the high carbon austenite only forms in ferritic ductile iron at the highest peak temperatures, while high carbon austenite in pearlitic ductile iron occurs over the entire range of peak temperatures, increasing as peak temperature increases.

In actual practice, manual welding employing a 600 - 800°F preheat, particularly on large components, is not feasible due to the hazardous condition presented to the welder. Even preheating localized areas for repair to these temperatures could induce cracking due to thermal stress and/or distortion. In such instances, a preheat of 400°F would be more practical. However, a preheat of 400°F would still result in a mixed microstructure of martensite and pearlite at some peak temperatures. This martensite could cause cracking at these preheats depending upon factors such as geometry of the component, size, restraint, etc. Therefore, each particular welding application must be analyzed to assess minimum preheat temperature requirements.

Austempered Condition

When the as-welded structures are subjected to the austemper heat treat process, the HAZ microstructure appears to be recoverable. This is demonstrated by the uniformity of hardness results (figs. 40 and 41) for each of the energy inputs. The recoverability of the PFZ, however, is not complete as is evident in figures 35 and 36. Although the hardness data does not suggest a difference in the PFZ austempered structure, the photomicrographs indicate a difference in structure exists.

The 100 min austenitizing time at 1650°F in austemper heat treat cycle is clearly sufficient time at temperature for carbon diffusion within the entire iron silicon matrix. The diffusion of carbon throughout the entire matrix allows for redistribution of carbon in austenite to an equilibrium 1650°F condition. This effectively erases the prior carbon concentration gradients existing in the arrested austenitic structures of the simulated weld heat affected zone. When incipient melting of the PFZ occurs, nodules are consumed upon the formation of liquid. This is apparent in figures 26 and 27, where eutectic forms in the vicinity of prior nodules. The silicon in the iron/silicon matrix drives the formation of secondary graphite particles. These particles are finely distributed throughout the iron/silicon matrix as shown in the scanning electron photomicrograph (fig. 37). These carbon particles represent prior localized regions of excess carbon concentration which may affect the bainitic transformation process

during the austemper heat treatment. The excess carbon concentration seems to affect volume fraction of reacted austenite as shown in figures 35 and 36. This was not confirmed through x-ray analysis, however.

The scope of this work revolved primarily around investigation of recoverability of the heat affected zone. The limited work in the partial fusion zone and fusion zone was due partially to the geometry of the Gleeble test specimen as already mentioned, but primarily to the fact that a second phase effort would study the PFZ/FZ. The first phase was designed to provide a foundation of knowledge about behavior of the HAZ for this second phase effort. The examples of significant melting, namely the 2148°F peak temperatures and the case of complete melting, were not austempered to investigate their recoverability. It is probable that they will react to austempering similarly to the 2100°F case of incipient melting. Upon austempering, the silicon in the iron/silicon matrix drives the formation of finely distributed graphite from the eutectic carbide. This should continue as the volume fraction of eutectic structure increases to the point of complete melting.

CONCLUSIONS

The austemper heat treat process is apparently effective in recovering the heat affected zone of the simulated as-welded microstructures, as is suggested by the hardness data and metallographic observations. However, the austemper heat treat process is not entirely effective in recovering microstructures in the partial fusion zone (PFZ)/fusion zone (FZ). This effect is only evident through metallographic observations using a scanning electron microscope as indicated by secondary graphite finely distributed through the matrix. The hardness data does not reflect any difference due to these particles.

The condition of the material prior to simulated weld thermal cycles has an effect on the as-welded condition of the microstructure. Other authors have shown that ferritic grades of ductile iron develop grain boundary carbides in the heat affected zone, while this work has demonstrated that a pearlitic prior microstructure in austempered ductile iron will not develop grain boundary carbides in the HAZ. This is desirable in reducing the possibility of HAZ cracking.

Controlling the cooling rate is another effective means of reducing the possibility of HAZ cracking. Cooling rate is a function of energy input and preheat temperature, so preheat temperature must be increased as energy input decreases so that a critical cooling rate of 6.3°F/s is not exceeded. Preheat temperature cannot increase without bound, however, as increasing preheat temperature increases the width of the PFZ and FZ, thus increasing the amount of melting and eutectic carbide. This potentially increases the amount of structure which may be unrecoverable through austemper heat treatment.

The recoverability was measured in terms of hardness and metallographic results only, and this is not complete with respect to actual weld joint performance. More extensive work is required to determine actual mechanical properties of the HAZ,PFZ, and FZ. Evaluation of tensile strength, yield strength, and elongation may better determine the extent of recovery achieved through austemper heat treatment.

FUTURE WORK

Based on the information obtained in the phase I effort, actual weld trials will be performed. The weld trials will be performed on a 1/2 in. plate at selected preheat temperatures for the 22.5 kJ/in. and 37.5 kJ/in. energy inputs using three different filler metals. A single v-groove weld will be prepared in both as-cast ferritic and pearlitic material to investigate the effect of prior material condition, preheat, and energy input on transverse mechanical properties of the austempered weld joint. This will quantify the recoverability of both the ferritic and pearlitic starting material as well as provide new information on the behavior of the fusion zone and the effect of filler metal on mechanical properties.

Additional weld trials will be performed on austempered 1/2 in. plate. Transverse mechanical properties of the as-welded material will be documented as part of this additional effort. This applies to field repair of austempered ductile iron which cannot be heat treated after welding.

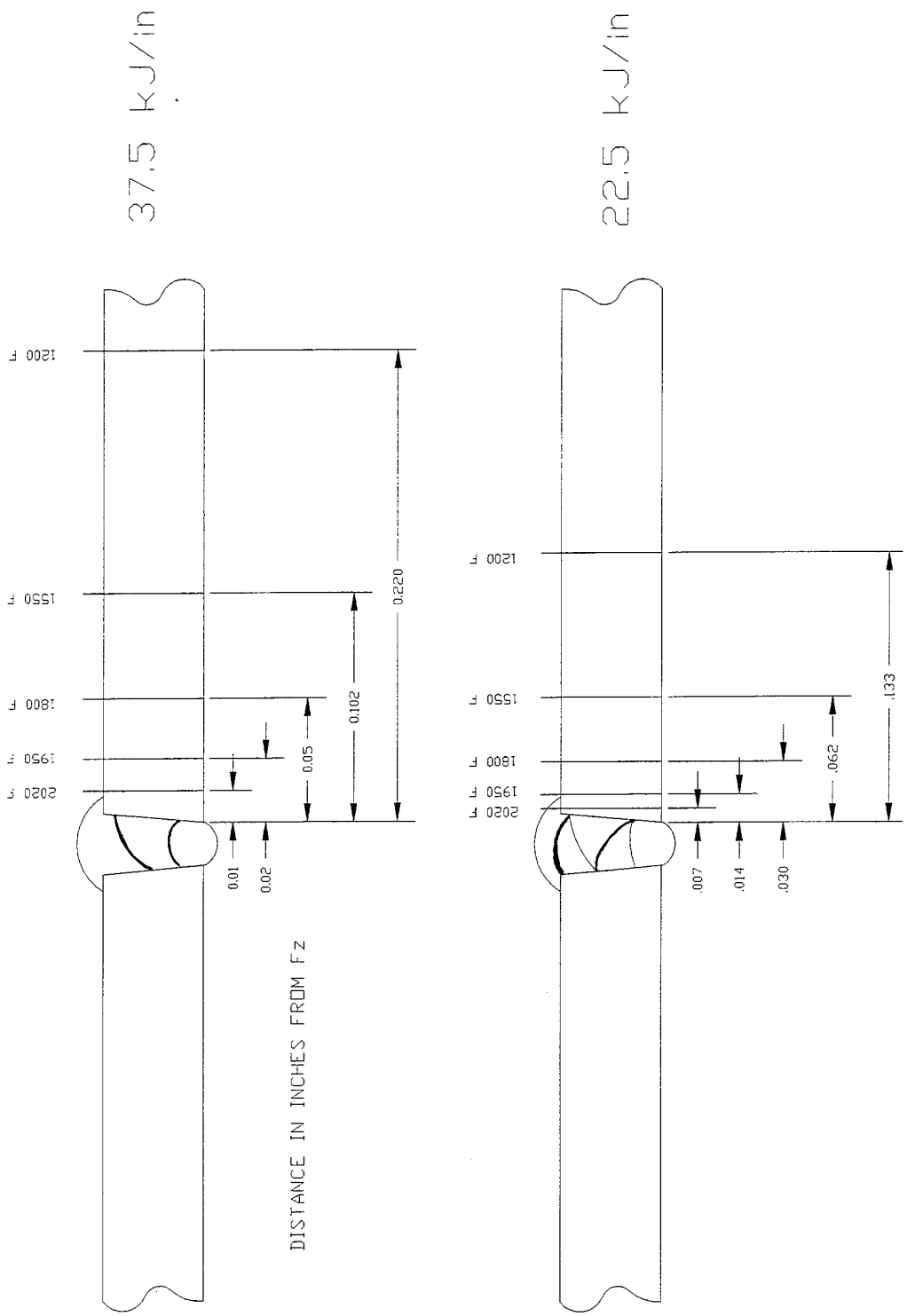

Figure 1
2D representation of weld HAZ

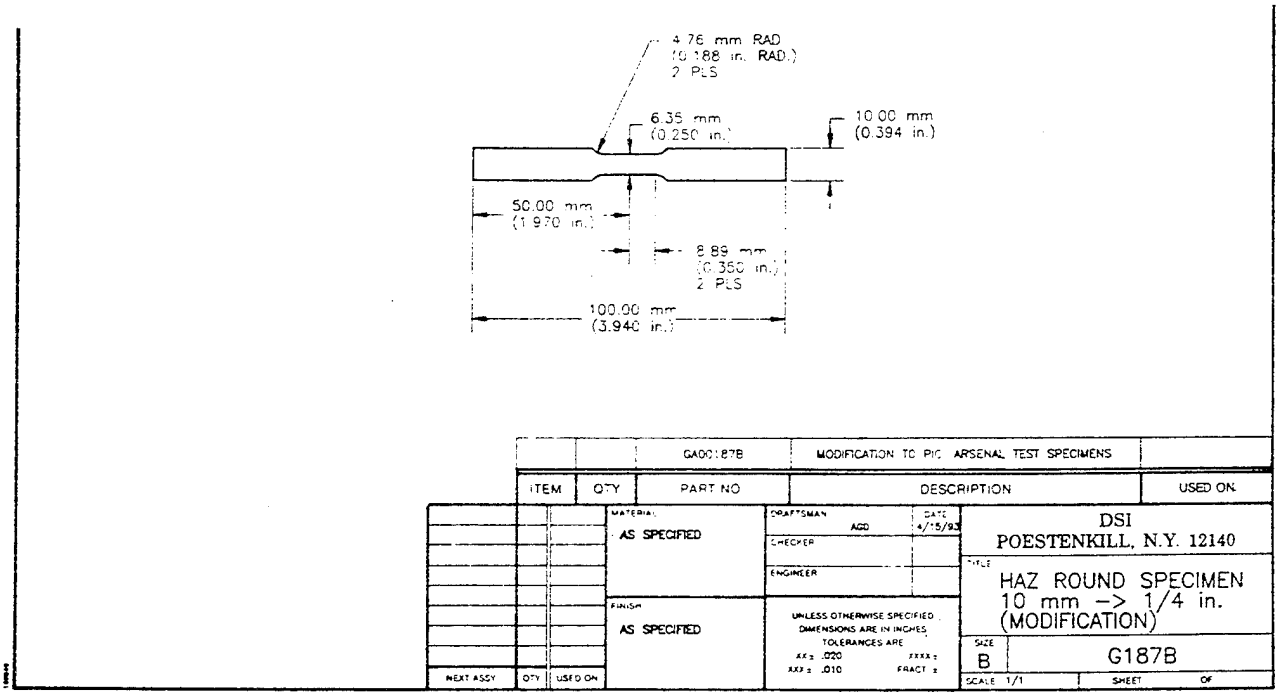

Figure 2
Gleeble test specimen

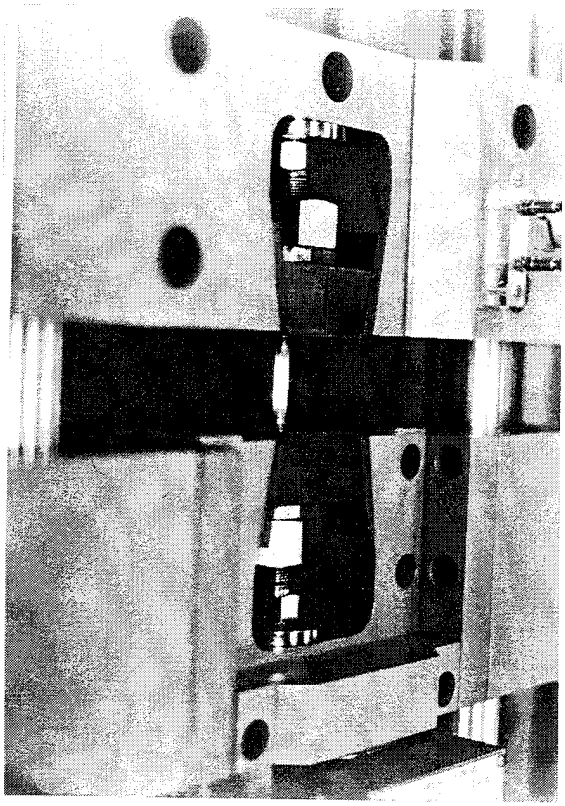

Figure 3
Photograph of Gleeble test apparatus

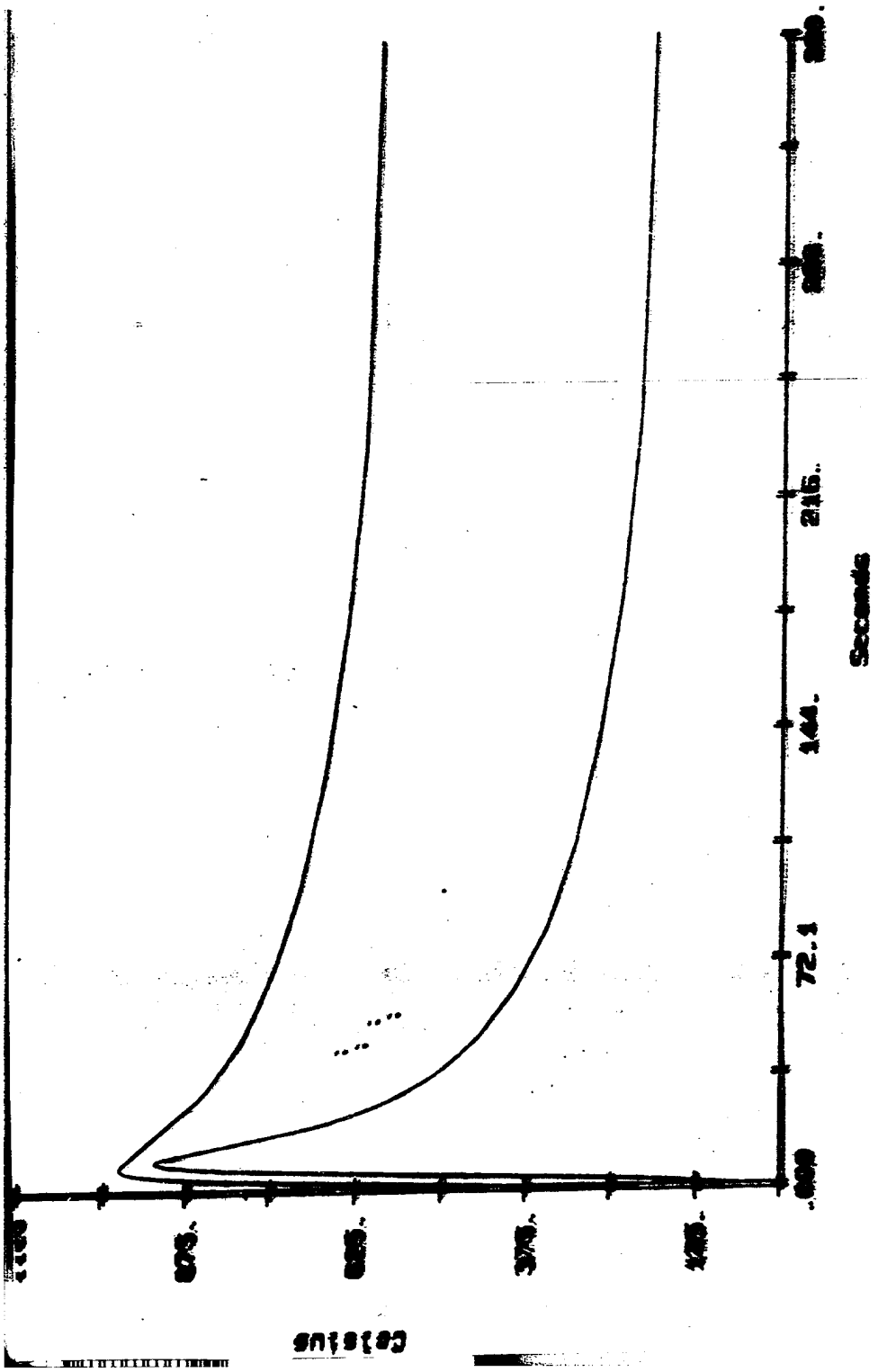

Figure 4
Experimental cooling curves at 1800°F peak temperature

Peak temperature / Preheat temperature	1200°F	1550°F	1800°F	1950°F	2020°F	2100°F
72°F	x/o	x/o	x/o	x/o	x/o	x/o
210°F			x/o	x/o	x/o	
400°F		x/o	x/o	x/o	x/o	
600°F		x/o	x/o	x/o	x/o	
800°F		x/o	x/o	x/o	x/o	

x = 37.5 kJ/in. energy input
o = 22.5 kJ/in. energy input

Figure 5
Experimental matrix

Figure 6
As-cast material as received from wager castings

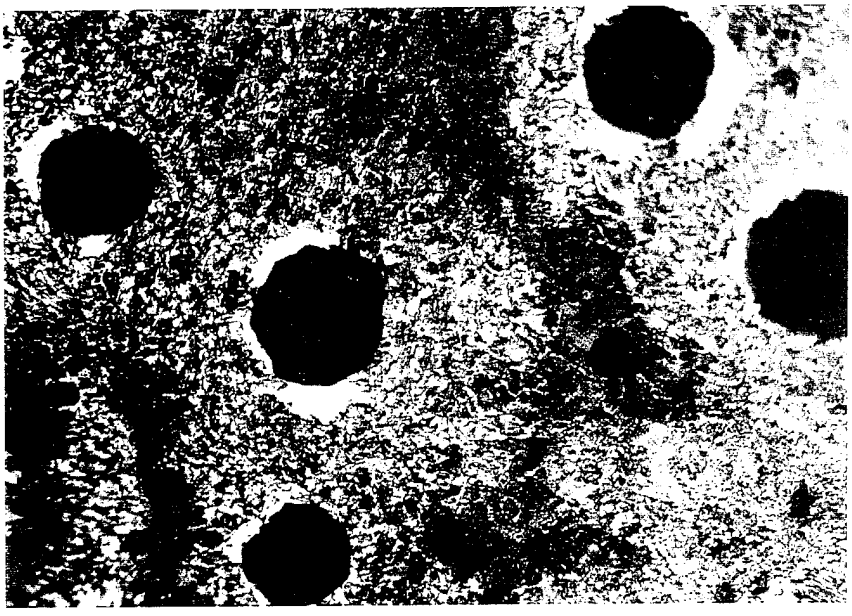

Figure 7
1550°F peak temperature, no preheat, 37.5 kJ/in.

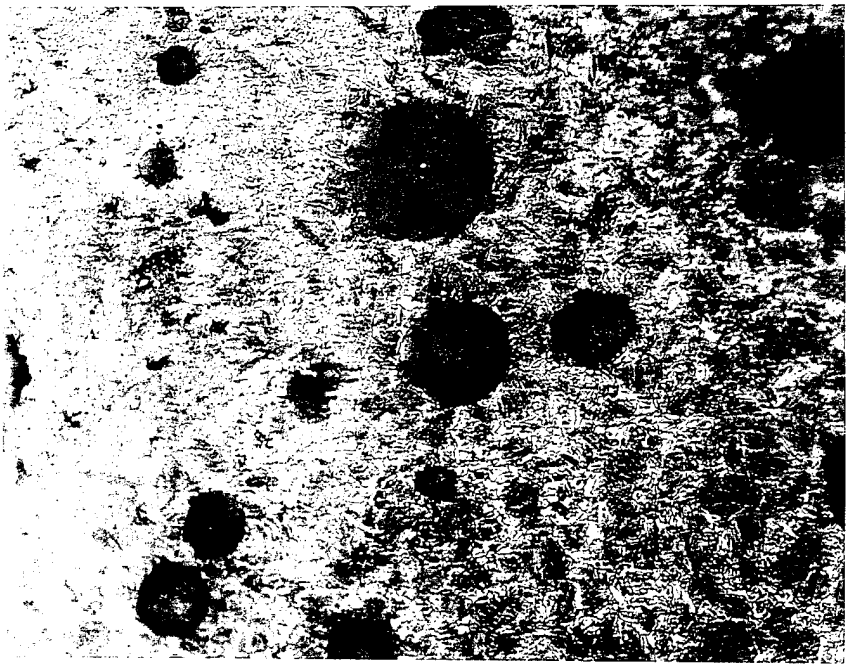

Figure 8
1800°F peak temperature, no preheat, 37.5 kJ/in. mixed microstructure of martensite, pearlite, and ferrite

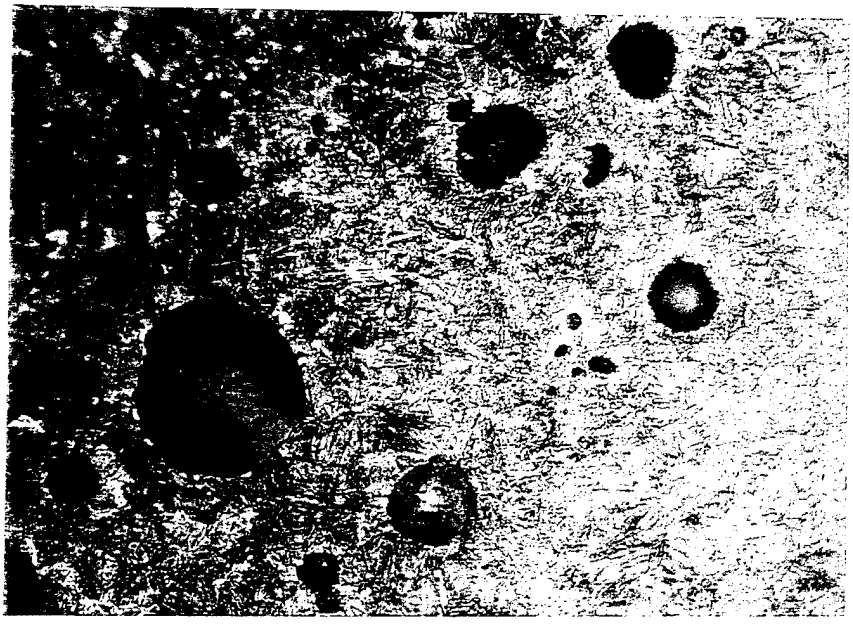

Figure 9
1950°F peak temperature, no preheat, 37.5 kJ/in. lath-like martensite evident

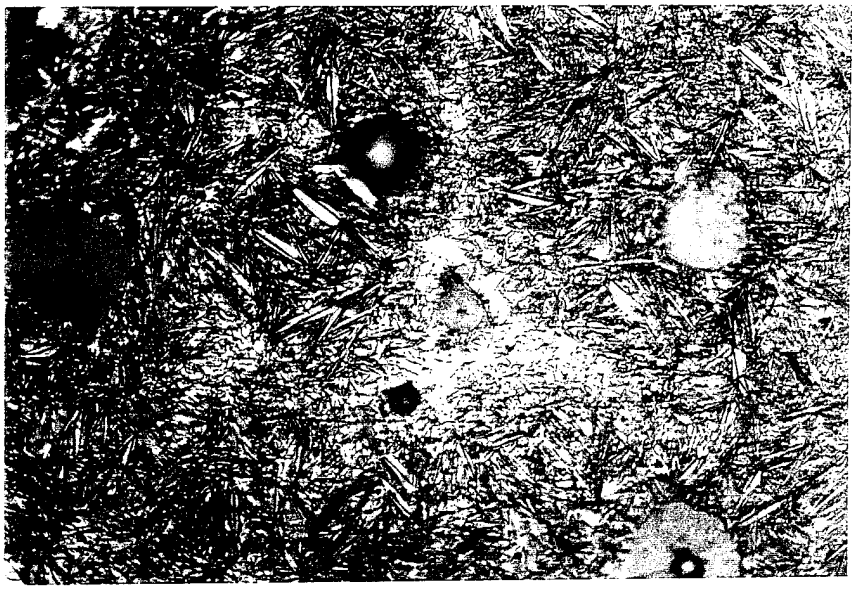

Figure 10
2020°F peak temperature, no preheat, 37.5 kJ/in. plate-like martensite and retained austenite

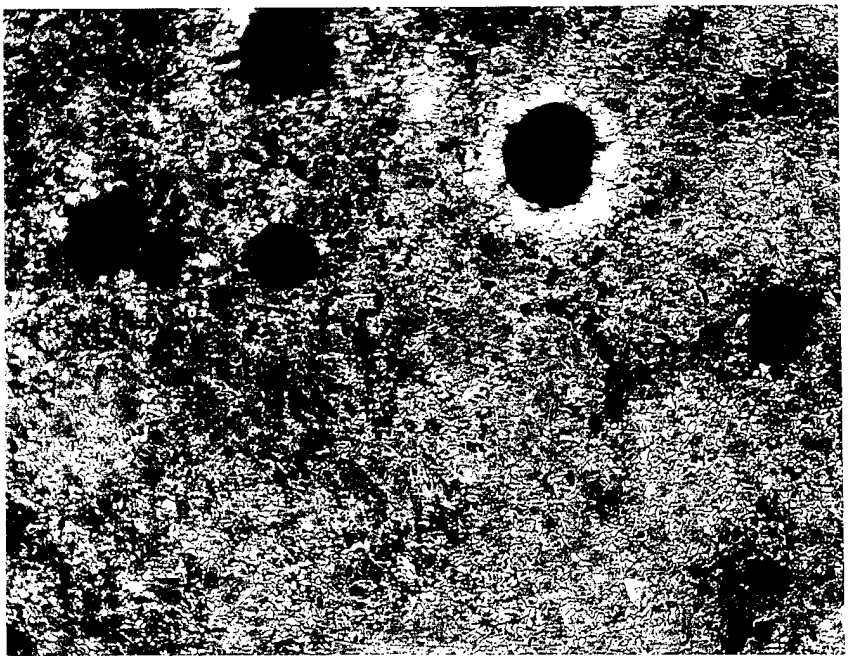

Figure 11
1550°F peak temperature, no preheat, 22.5 kJ/in. martensite, ferrite, and pearlite

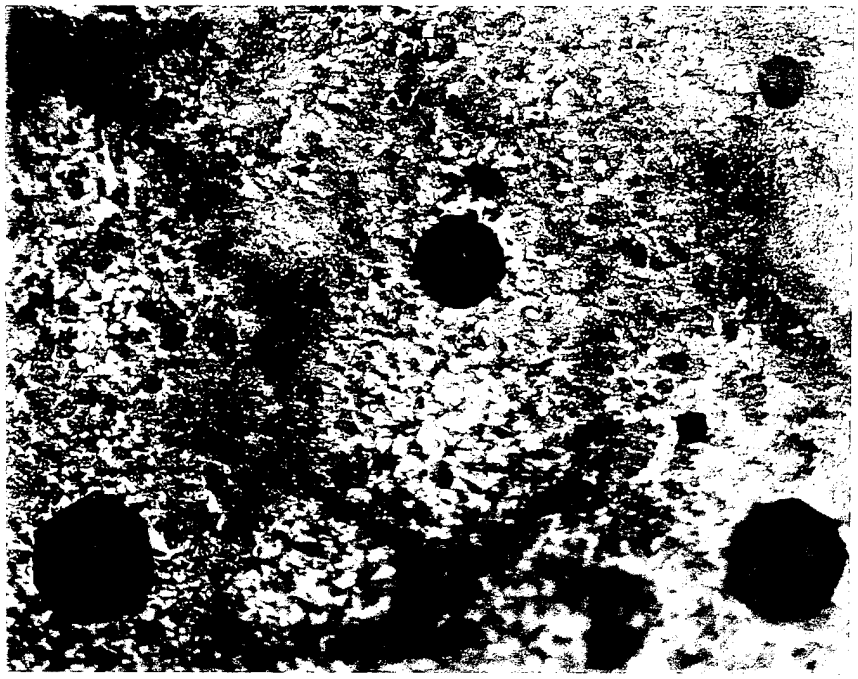

Figure 12
1550°F peak temperature, 600°F preheat, 22.5 kJ/in. coarse pearlite and proeutectoid ferrite

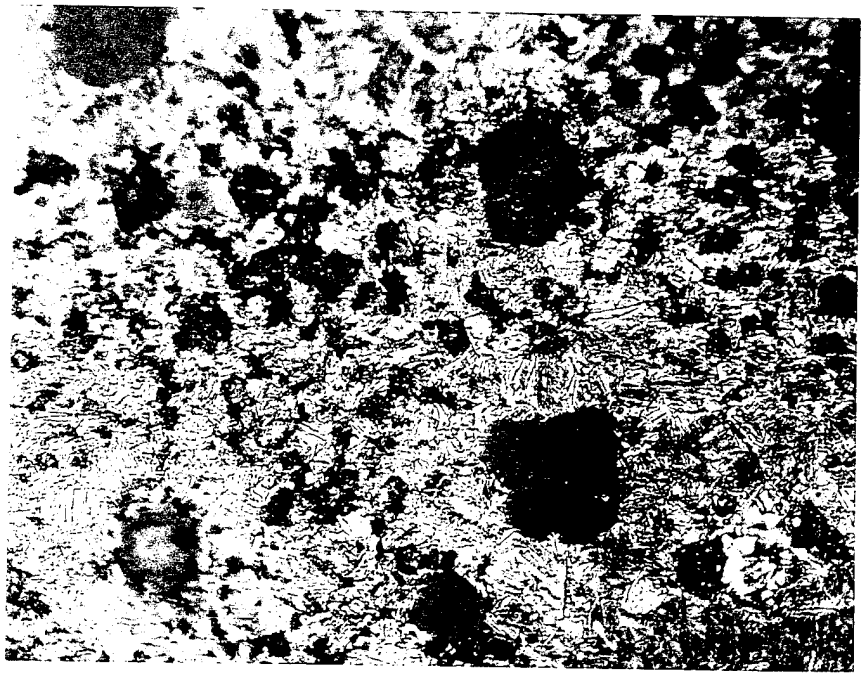

Figure 13
1950°F peak temperature, 400°F preheat, 37.5 kJ/in. ferrite and pearlite

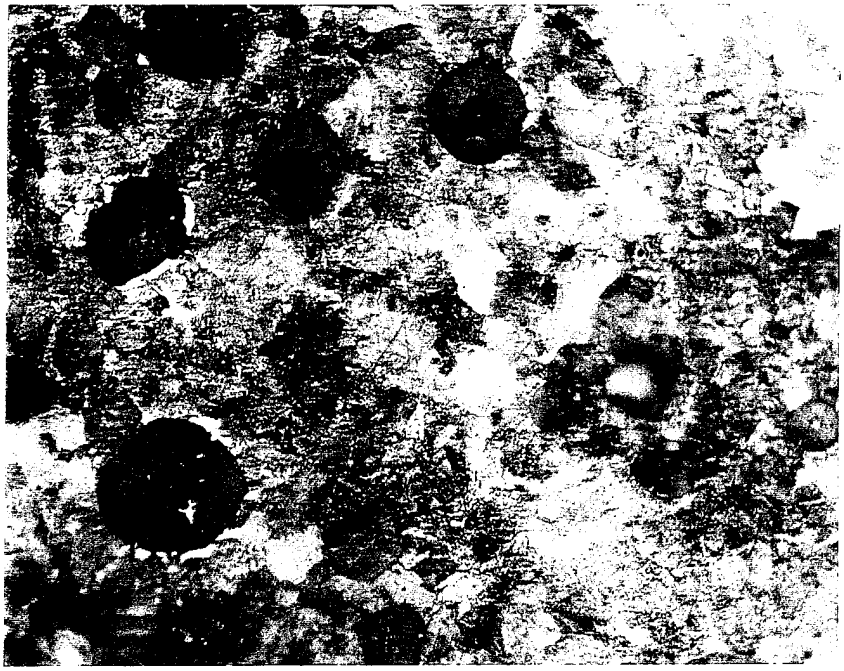

Figure 14
1950°F peak temperature, 600°F preheat, 37.5 kJ/in. pearlite

Figure 15
1950°F peak temperature, 800°F preheat, 37.5 kJ/in. pearlite

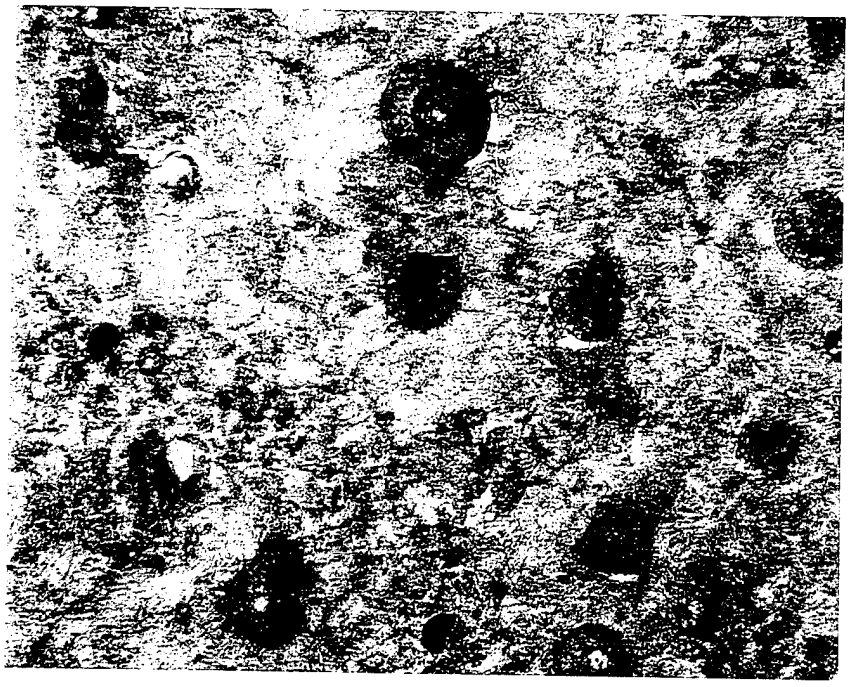

Figure 16
1950°F peak temperature, 800°F preheat, 22.5 kJ/in. pearlite

Figure 17
2020°F peak temperature, 400°F preheat, 37.5 kJ/in. martensite with some pearlite

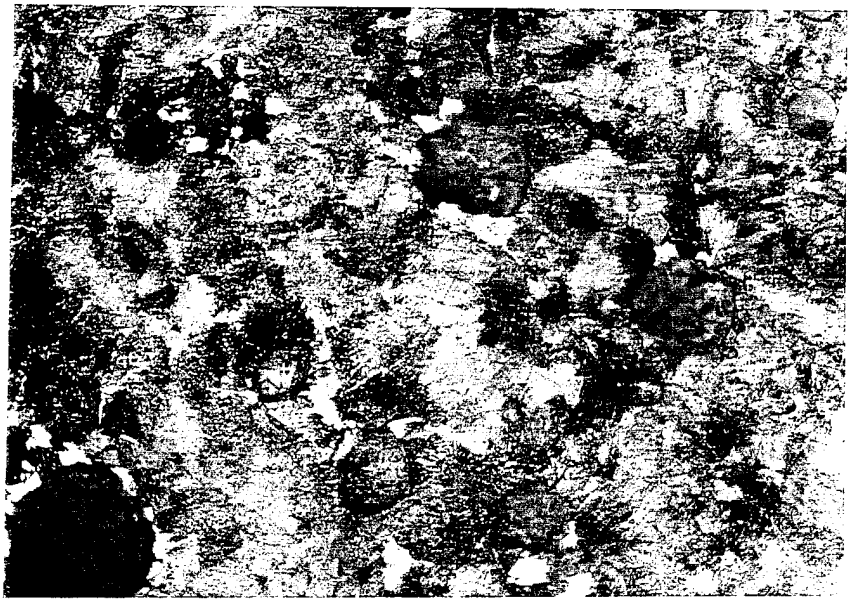

Figure 18
2020°F peak temperature, 600°F preheat, 37.5 kJ/in. pearlite

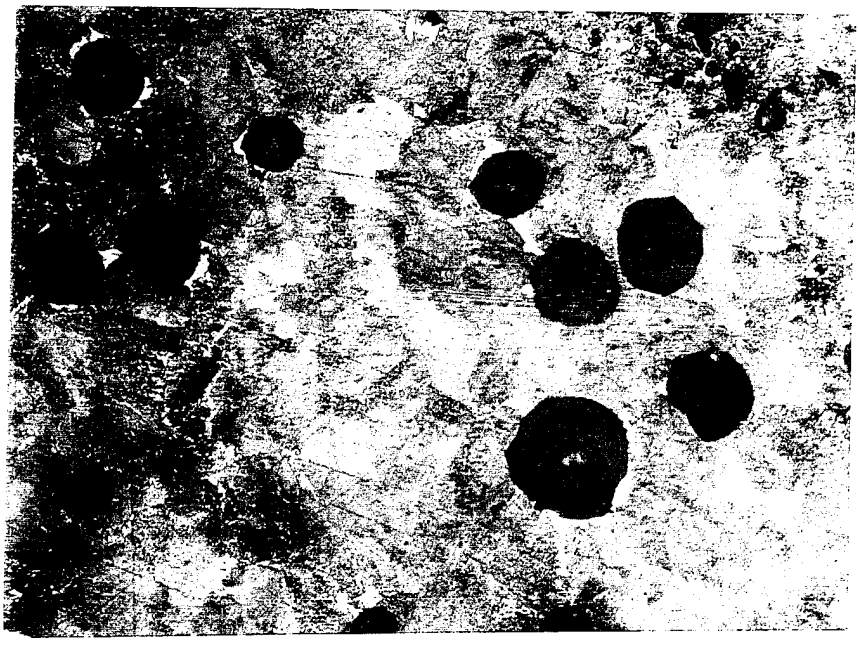

Figure 19
2020°F peak temperature, 800°F preheat, 37.5 kJ/in. pearlite

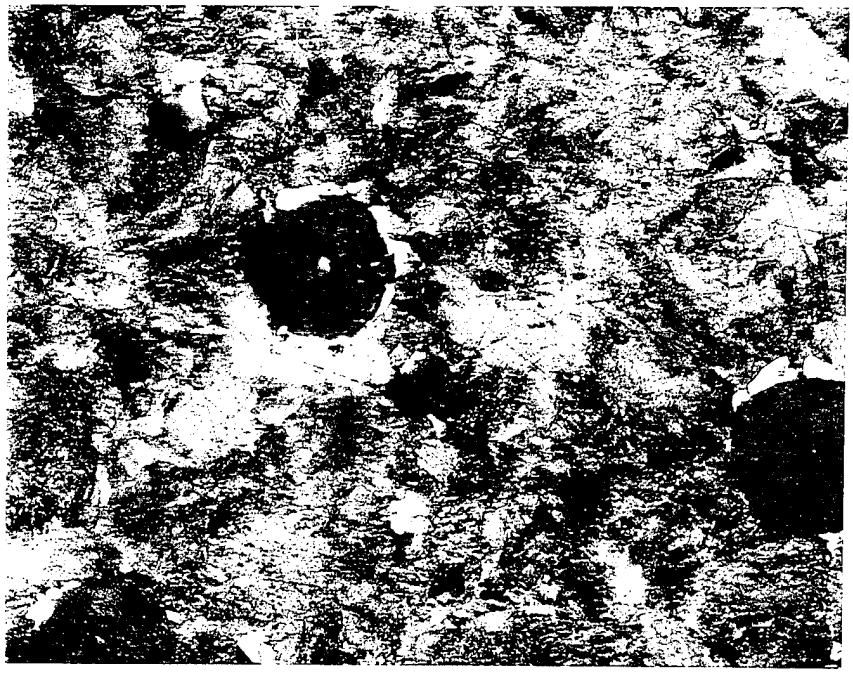

Figure 20
2020°F peak temperature, 800°F preheat, 22.5 kJ/in. pearlite

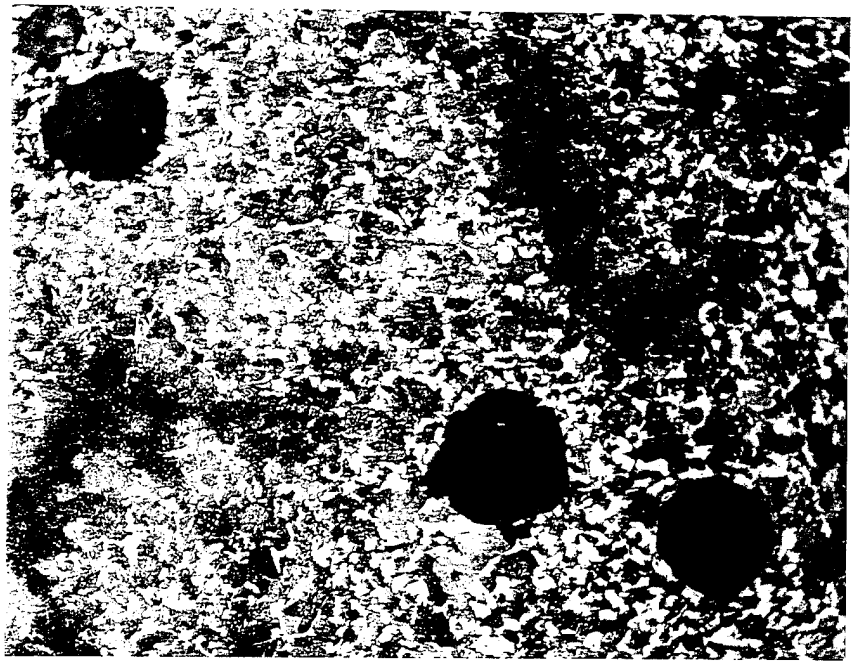

Figure 21
1800°F peak temperature, 600°F preheat, 37.5 kJ/in. fine pearlite at austenitic grain boundaries with blocky ferrite and pearlite

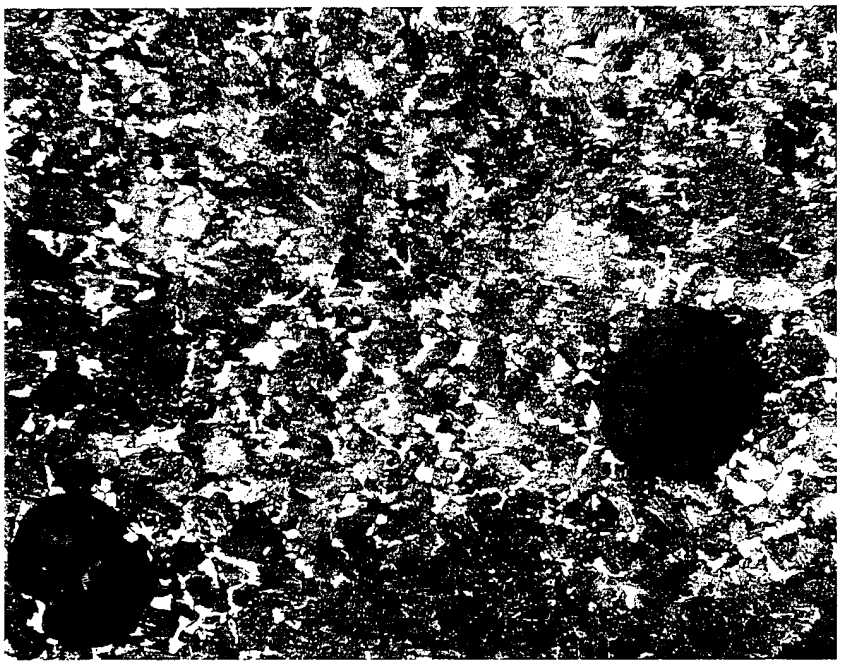

Figure 22
1800°F peak temperature, 800°F preheat, 22.5 kJ/in.
fine pearlite, block ferrite, and pearlite

Figure 23
1800°F peak temperature, 800°F preheat, 37.5 kJ/in. fine pearlite

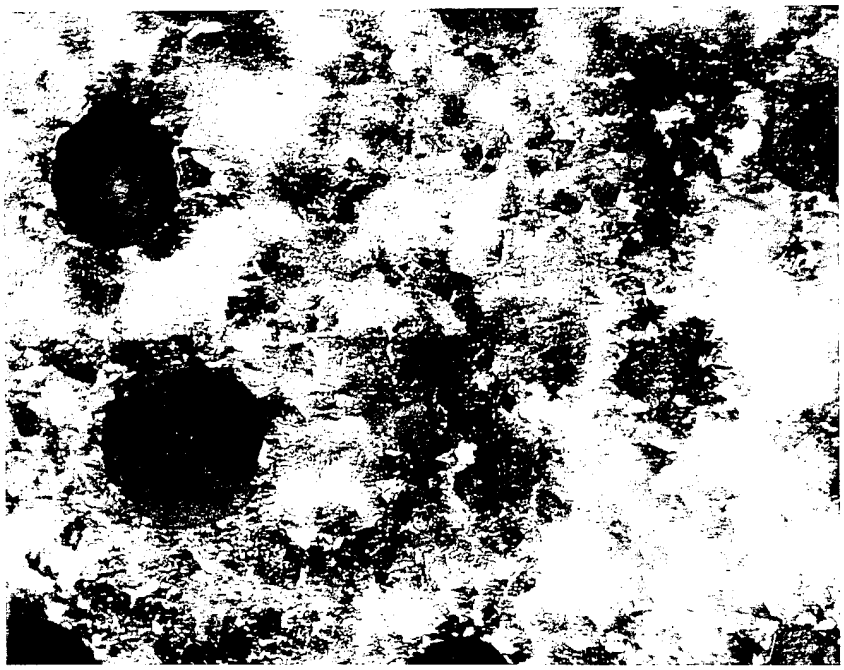

Figure 24
1800°F peak temperature, 600°F preheat, 22.5 kJ/in.
Widmanstätten ferrite and martensite magnified 500 times

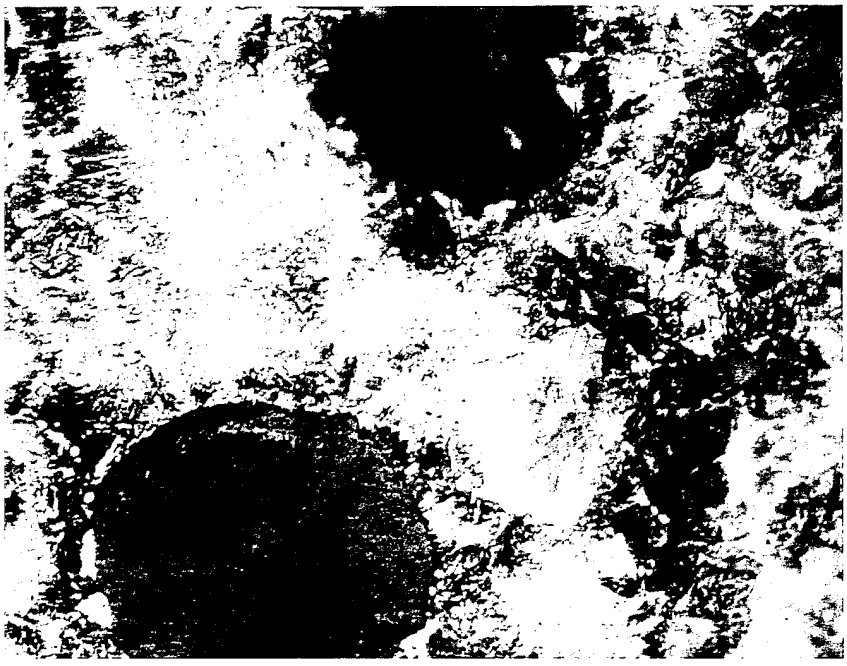

Figure 25
1800°F peak temperature, 600°F preheat, 22.5 kJ/in.
Widmanstätten ferrite and martensite magnified 1000 times

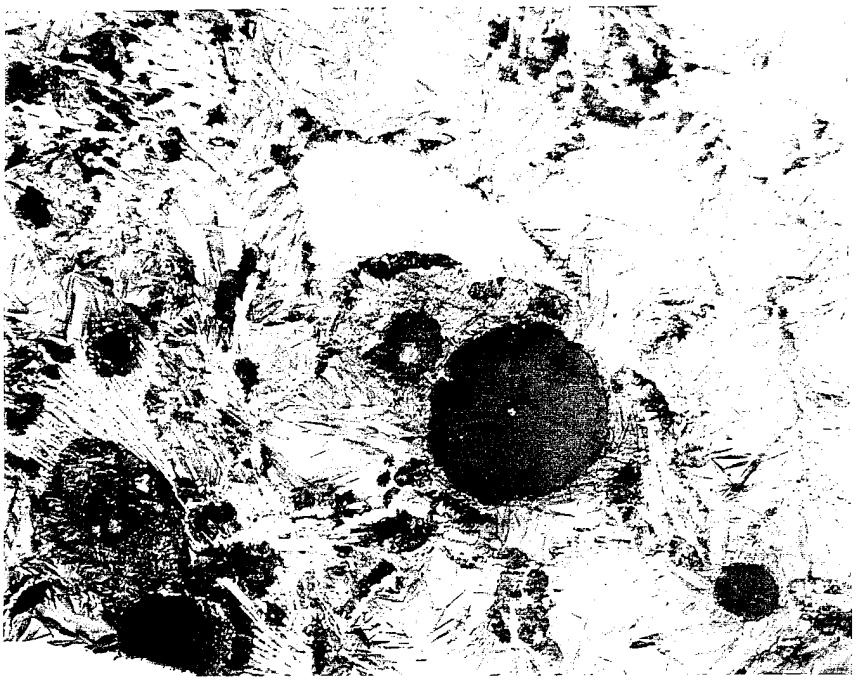

Figure 26
2100°F peak temperature, no preheat, 37.5 kJ/in.
eutectic carbide, plate martensite, and retained austenite

Figure 27
2100°F peak temperature, no preheat, 22.5 kJ/in.
eutectic carbide, plate martensite, and retained austenite

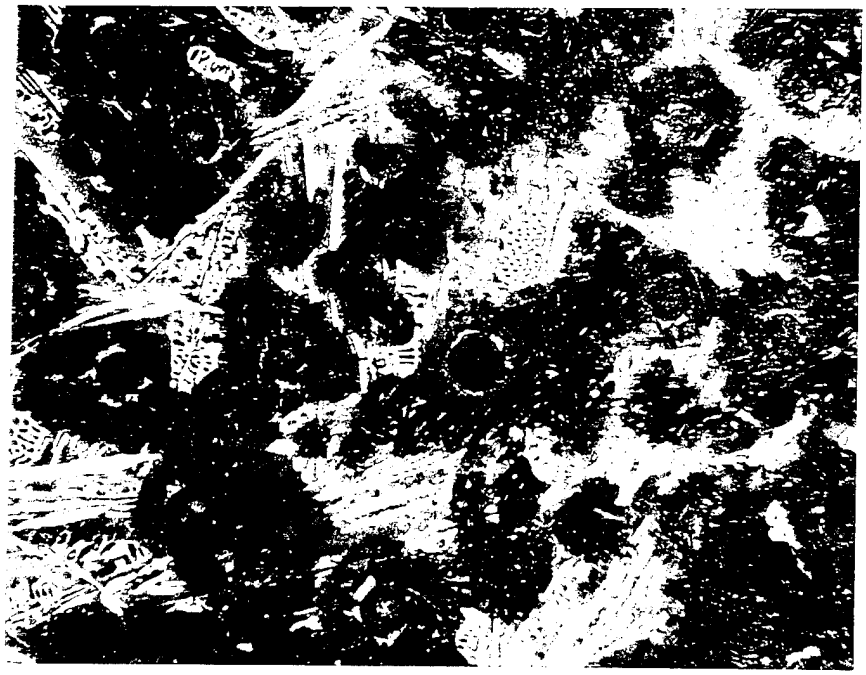

Figure 28
2148°F peak temperature, no preheat, 37.5 kJ/in.
transformed ledeburite, eutectic carbide, and martensite

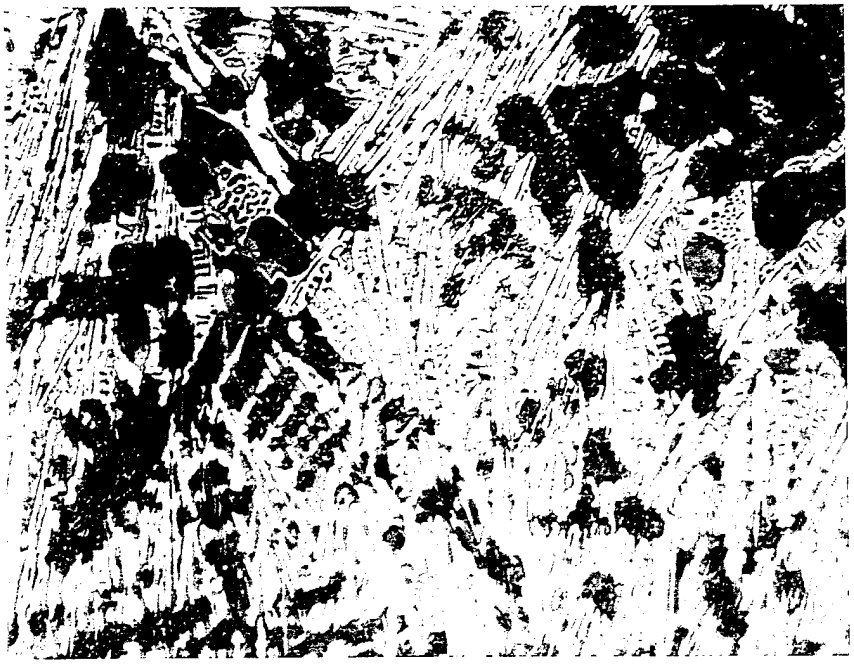

Figure 29
Example of complete melting, eutectic carbide and martensite
graphite nodules completely dissolved

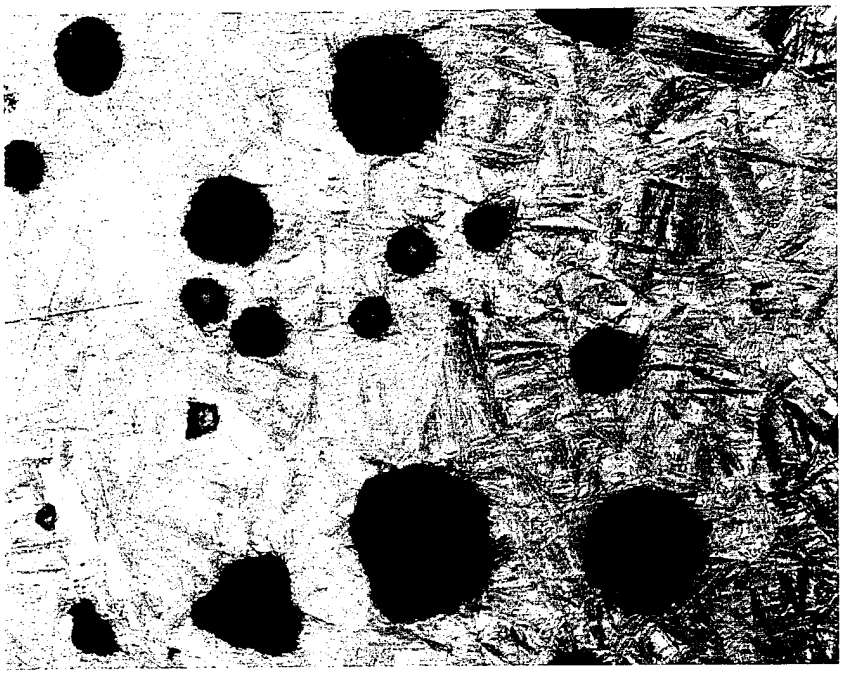

Figure 30
Austempered as-cast microstructure bainitic ferrite and reacted austenite

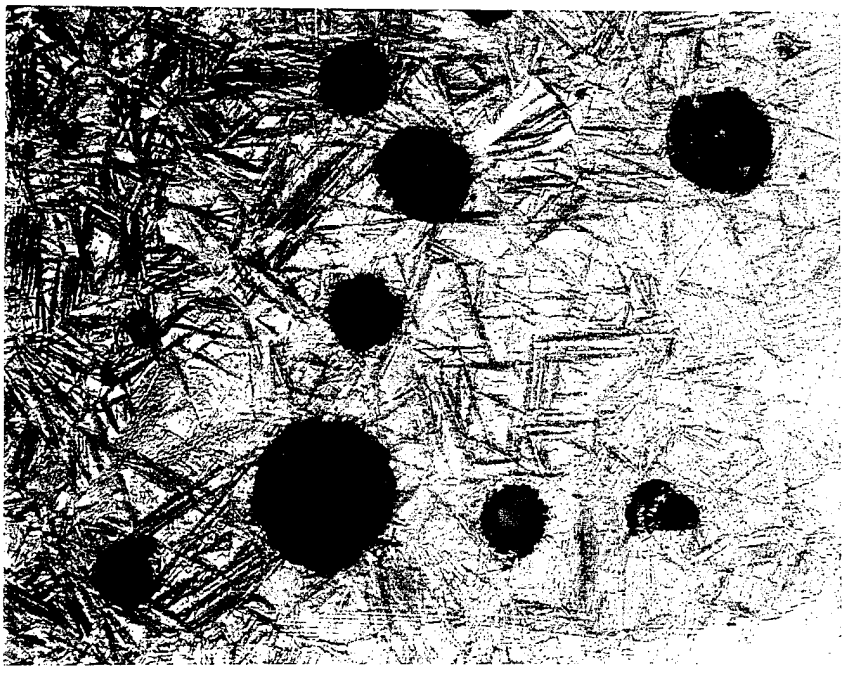

Figure 31
1550°F peak temperature, 400°F preheat, 37.5 kJ/in. coarse bainitic microstructure

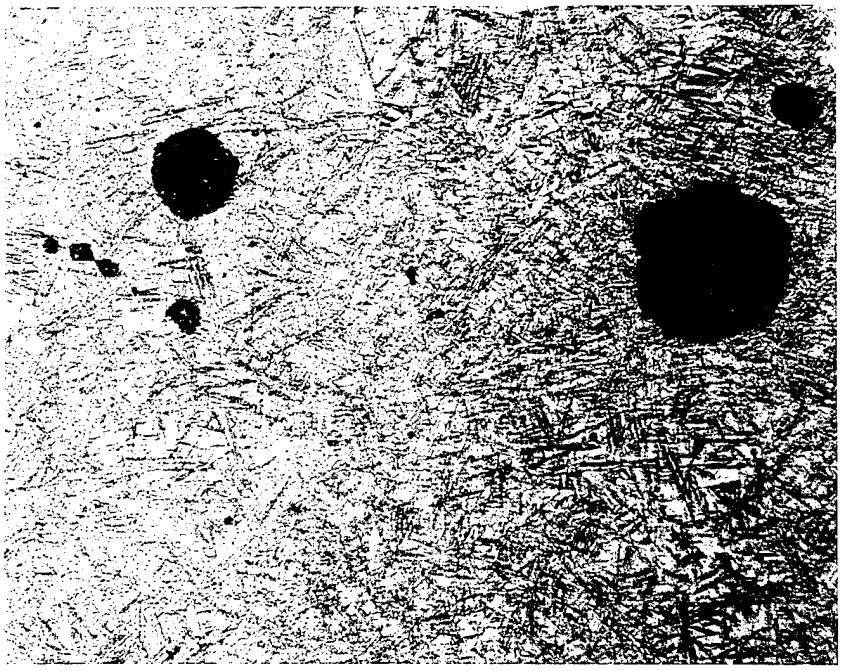

Figure 32
1950°F peak temperature, 210°F preheat, 37.5 kJ/in. fine bainitic microstructure

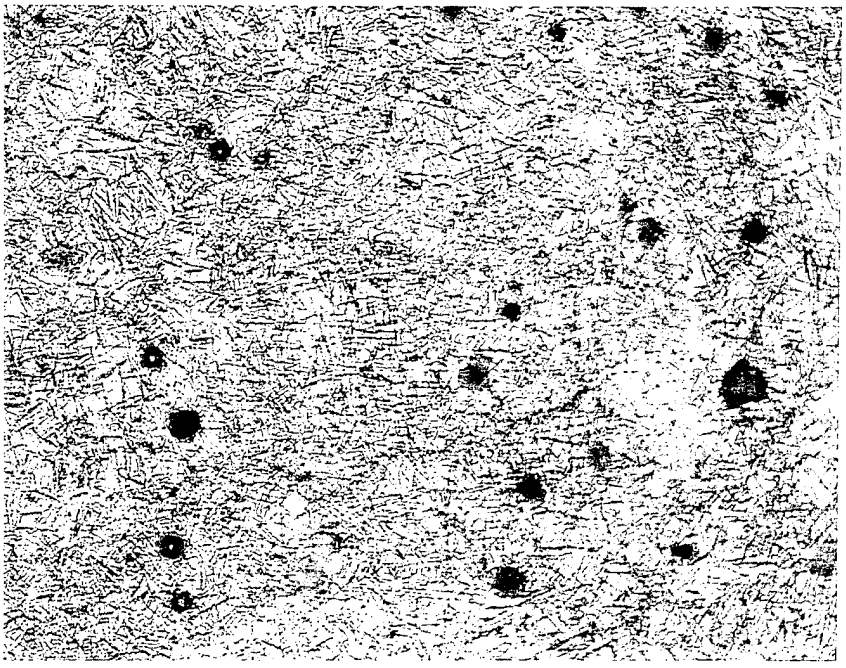

Figure 33
2100°F peak temperature, no preheat, 37.5 kJ/in.
effect of incipient melting on austempered structure

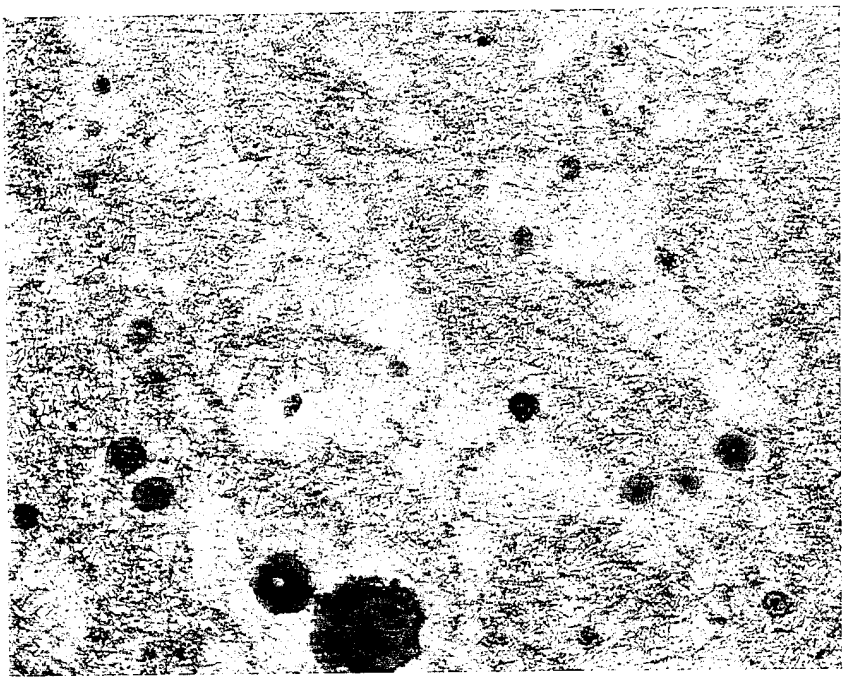

Figure 34
2100°F peak temperature, no preheat, 22.5 kJ/in.
effect of incipient melting on austempered structure magnified 500 times

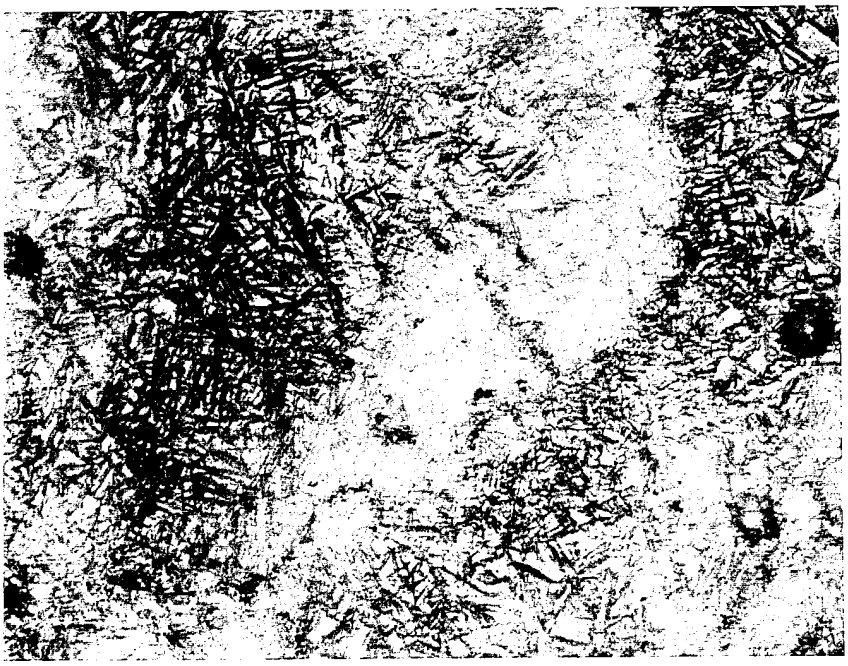

Figure 35
2100°F peak temperature, no preheat, 37.5 kJ/in.
effect of incipient melting on austempered structure magnified 1000 times

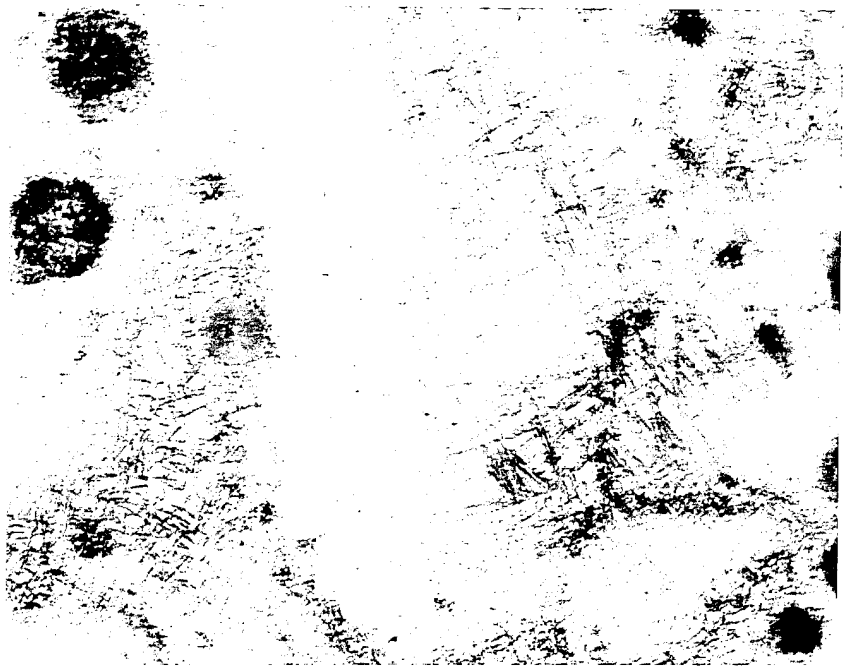

Figure 36
2100°F peak temperature, no preheat, 22.5 kJ/in.
effect of incipient melting on austempered structure magnified 1000 times

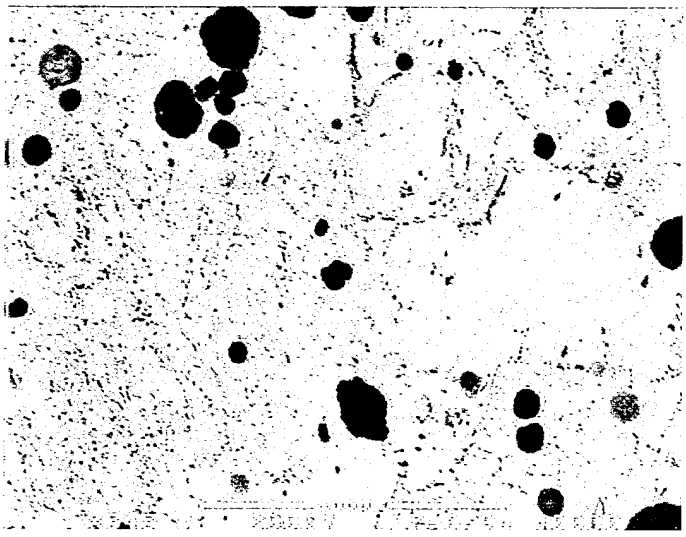

Figure 37
2100°F peak temperature, no preheat, 37.5 kJ/in.
SEM backscattered photomicrograph showing secondary graphite

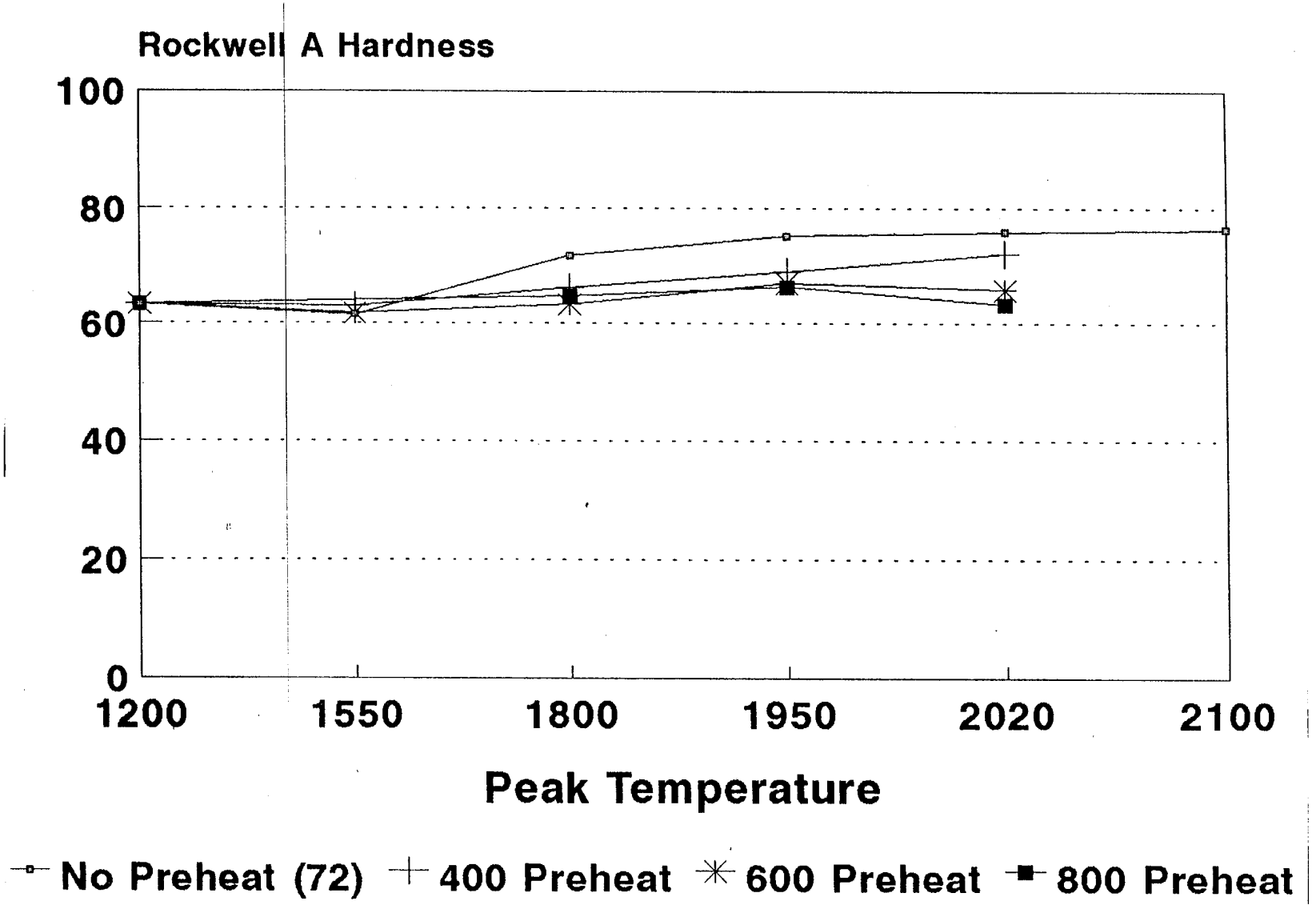

Figure 38
Rockwell A hardness - 37.5 kJ/in., as-welded

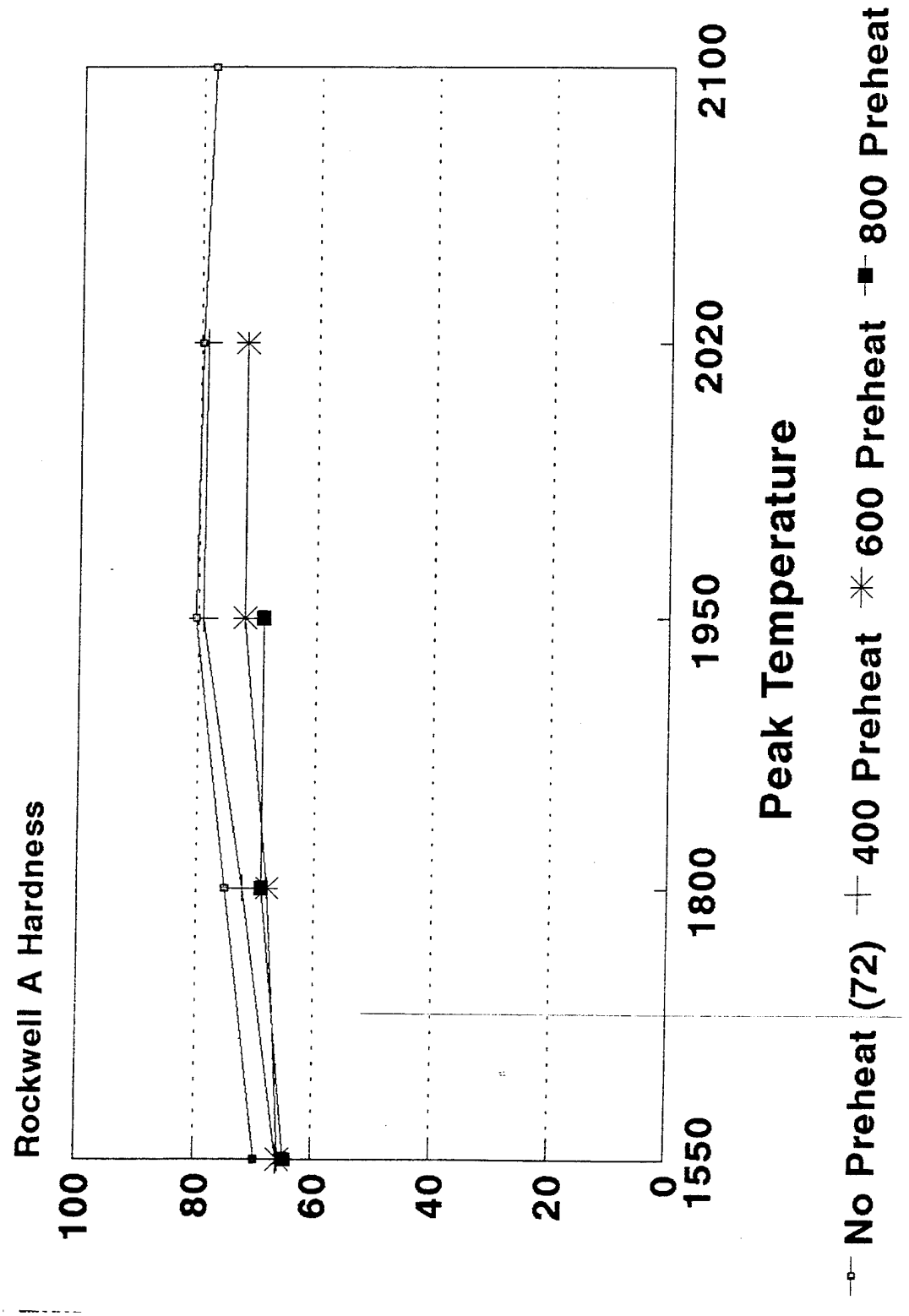

Figure 39
Rockwell A hardness - 22.5 kJ/in., as-welded

Figure 40
Rockwell A hardness - 37.5 kJ/in., austempered

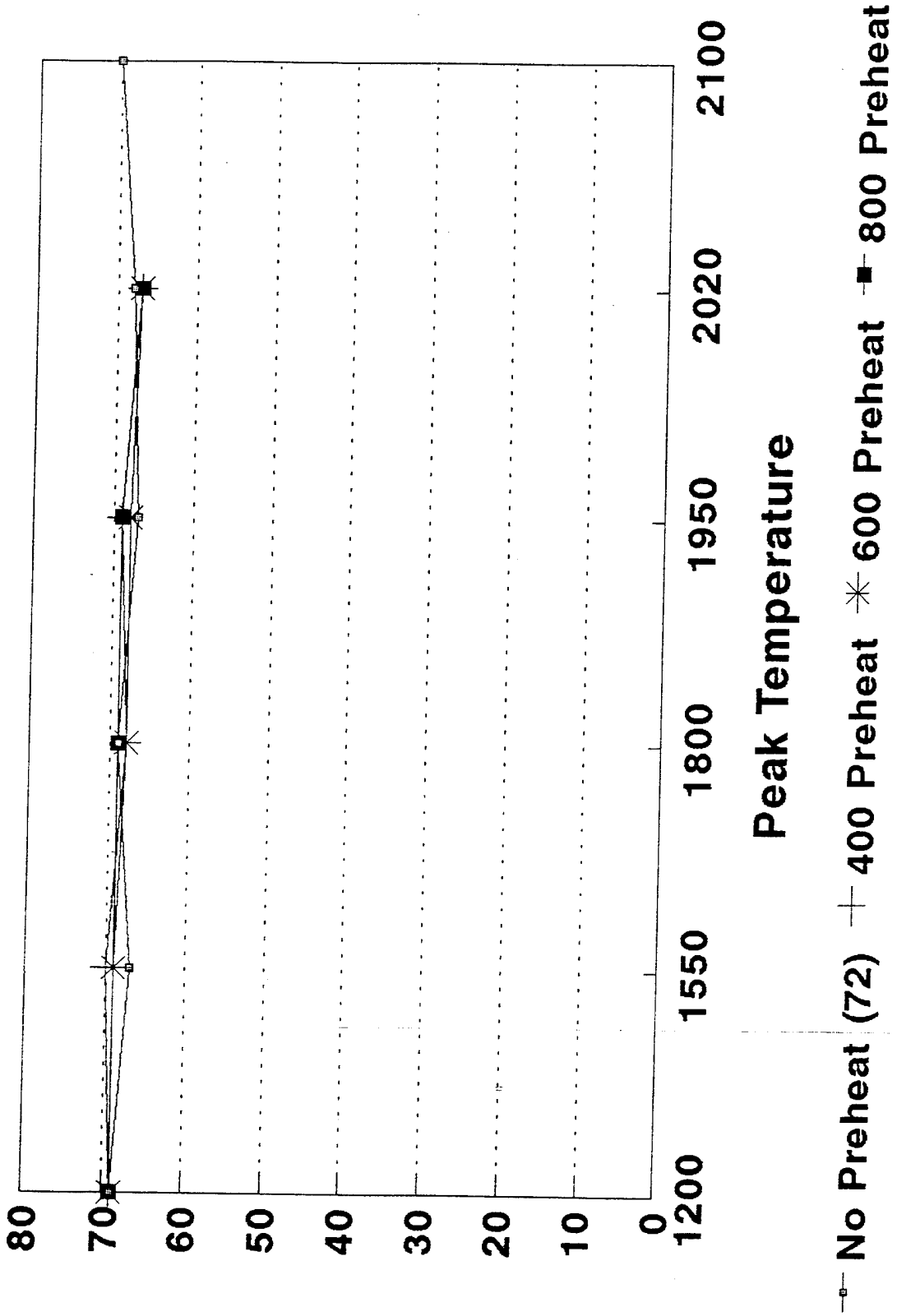

Figure 41
Rockwell A hardness - 22.5 kJ/in., austempered

Table 1
Typical chemistry

C	Si	Mn	Cr	Al	S	P	Cu	Ni	Ti	Mo	Mg
3.71	2.62	0.27	0.035	0.015	0.010	0.008	0.876	0.818	0.005	0.002	0.047

Table 2
Heat treatment parameters

Condition	Temperature (°F)	Time (min)
Stress relieve	1100	90
Austenitize	1640+/-5	100
Quench and isothermal	625+/-5 Hold	100

Table 3
Average mechanical test results (austempered)

Yield strength (psi)	Tensile strength (psi)	Percent elongation
140,000	184,000	8.0%

Table 4
Cooling rate - °F/s at 1300°F

Initial plate Temperature	Cooling Rate	
	37.5 kJ/in. (°F/s)	22.5 kJ/in. (°F/s)
72	34.0	94.5
210	23.7	66.0
400	13.4	37.2
600	6.3	17.5
800	2.3	6.3

REFERENCES

1. Nippes, E.F., Savage W.F., and W.A. Owczarski, The Heat-Affected Zone of Arc-Welded Ductile Iron, Welding Journal, Research Supplement, 465s-472s, 1960.

2. "Austempered Ductile Iron Database," A Cooperative Program Between Industry and the Trade Adjustment Assistance Program of the Department of Commerce, PB90-115569 (1989), Chapter 2 Austenite Transformation Characteristics, 1989.

3. "Austempered Ductile Iron Database," A Cooperative Program Between Industry and the Trade Adjustment Assistance Program of the Department of Commerce, PB90-115569 (1989), Chapter 3 Microstructures After Heat Treatment.

4. Kotecki, D.J., Braton, N.R. and C.R. Roper Jr., Preheat Effects on Gas Metal-Arc Welded Ductile Cast Iron, Welding Journal Research Supplement.

BIBLIOGRAPHY

1. Bain, Edgar and Harold W. Paxton, Alloying Elements in Steel, American Society for Metals, Metals Park, Ohio, 1966.

2. Krauss, George, Steels: Heat Treatment and Processing Principles, American Society for Materials, Materials Park, Ohio, 1990.

3. Porter, D.A. and K.E. Easterling, Phase Transformations in Metals and Alloys. Van Nostrand (U.K.), Workingham, Berkshire, England, 1981.

4. Rauch, A.H. (ed), Source Book on Ductile Iron, American Society for Metals, Metals Park, Ohio, 1977.

5. Walton, Charles F. (ed), The Gray Iron Castings Handbook, Cleveland, Ohio, 1958.

APPENDIX

CALCULATION DESCRIPTION - RYKALIN 2-D

Calculation Description - Rykalin 2-D

The "Rykalin" calculation methods are based on work by N. N. Rykalin. The equations used for Rykalin 2-D curves are shown below:

T_{Max} = Maximum temperature
T_0 = Preheat temperature
T_1, T_2 = Temperatures used to define cooling time.
d = Plate thickness
d_e = Equivalent plate thickness
t = Cooling time from T1 to T2
Q = Energy input
l = thermal conductivity
p = density
c = specific heat

$$Q = \sqrt{\frac{4\ PI\ lpc\Delta t}{\frac{1}{(T_2-T_0)^2} - \frac{1}{(T_1-T_0)^2}}}\ d$$

$$d_e = \sqrt{\frac{Q}{2pc}\left(\frac{1}{T_2-T_0} + \frac{1}{T_1-T_0}\right)}$$

$$r = \frac{Q}{T_{Max}dcp\sqrt{2\ PI\ e}}$$

$$T = \frac{Q}{d}\ \frac{1}{\sqrt{4\ PI\ lpct}}\ e^{-\frac{r^2}{4\ (\ l\ /\ pc)t}}$$

DISTRIBUTION LIST

Commander
Armament Research, Development and Engineering Center
U.S. Army Tank-automotive and Armaments Command
ATTN: AMSTA-AR-IMC (3)
AMSTA-AR-GCL
AMSTA-AR-CCH-P (10), William Sharpe
AMSTA-AR-AET-M (5), Roger Stanton
AMSTA-AR-CCH-D (5), George Scullin
AMSMC-PBR-M(D), Al Gonsiska
Ferdinand del Carmen
Picatinny Arsenal, NJ 07806-5000

Administrator
Defense Technical Information Center
ATTN: Accessions Division (12)
Cameron Station
Alexandria, VA 22304-6145

Director
U.S. Army Material Systems Analysis Activity
ATTN: AMXSY-MP
Aberdeen Proving Ground, MD 21005-5066

Commander
Chemical/Biological Defense Agency
U.S. Army Armament, Munitions and Chemical Command
ATTN: AMSCB-CII, Library
Aberdeen Proving Ground, MD 21010-5423

Director
U.S. Army Edgewood Research, Development and Engineering Center
ATTN: SCBRD-RTT (Aerodynamics Technical Team)
Aberdeen Proving Ground, MD 21010-5423

Director
U.S. Army Research Laboratory
ATTN: AMSRL-OP-CI-B, Technical Library
AMSRL-MA-CC, Martin Wells
Aberdeen Proving Ground, MD 21005-5066

Director
U.S. Army TRADOC Analysis Command-WSMR
ATTN: ATRC-WSS-R
White Sands Missile Range, NM 88002

Chief
Benet Weapons Laboratory, CCAC
Armament Research, Development and Engineering Center
U.S. Army Armament, Munitions and Chemical Command
ATTN: SMCAR-CCB-TL
SMCAR-CCB-SM, Alex Wakulenko
SMCAR-CCB-SE, Peter Thornton
SMCAR-CCB-RM, Paul Cote
SMCAR-CCB-RM, Edward Troiano
Watervliet, NY 12189-5000

Office of the Under Secretary of Defense for Research and Engineering
The Pentagon
Washington, D.C. 20301

Commander
Army Research Office
ATTN: Information Processing Office
P.O. Box 12211
Research Triangle Park, NC 27709-2211

Commander
U.S. Army Materiel Command
ATTN: AMCSCI
AMCRD-M
501 Eisenhower Avenue
Alexandria, VA 22333-0001

Commander
U.S. Army Tank-Automotive Command
ATTN: AMSTA-TSL, Technical Library
AMSTA-TMF, James W. Ogilvy
AMSTA-RTT, Robert Smith
Warren, MI 48397-5000

Commander
Rock Island Arsenal
ATTN: SMCRI-SEM-A, Cynthia Krist
SMCRI-SEM-T, Cesar Cardenas
Rock Island, IL 61299

Commander
U.S. Army Foreign Science and Technology Center
ATTN: AIFRTC, Applied Technologies Branch, Gerald Schlesinger
220 7th Street N.E.
Charlottesville, VA 22901-5396

Naval Research Laboratory
ATTN: Code 5830
Washington, D.C. 20375

Naval Sea System Command
ATTN: Code 03R5, John Williams
Washington, D.C. 20326-5101

Naval Surface Warfare Center
ATTN: Code G32, O.J. Huey
Dahlgren, VA 22448-5000

Commander
U.S. Air Force Wright Research and Development Center
ATTN: WL/MT-Bldg 653, Siamack Mazdiyasni
2977 P Street STE6
Wright Patterson Air Force Base, OH 45433-6523